Laboratory experiments simulating poroelastic stress changes associated with depletion and injection in low-porosity sedimentary rocks: ultrasonic velocities and dynamic effective stress coefficients

Xiaodong Ma[1,2], Mark D. Zoback[1] and Gary M. Mavko[1]

Author Contact Information

Xiaodong Ma *(corresponding author)*

[1]Stanford University, Department of Geophysics

397 Panama Mall Room B12, Stanford, CA 94305, USA

[2]ETH Zürich, Swiss Competence Center for Energy Research (SCCER-SoE)

NO F27, Sonneggstrasse 5, CH-8092 Zürich, Switzerland

Email: xiaodongma.rocks@gmail.com

Mark D. Zoback

[1]Department of Geophysics, Stanford University

397 Panama Mall Room 347, Stanford, CA 94305, USA

zoback@stanford.edu (650) 725-9295

Gary M. Mavko

[1]Department of Geophysics, Stanford University

397 Panama Mall Room 313, Stanford, CA 94305, USA

mavko@stanford.edu (650) 723-9438

ABSTRACT

We characterized the dependence of ultrasonic velocities on confining pressure (P_c) and pore pressure (P_p) of six argon-saturated cores from three formations associated with the Bakken play in the Williston Basin (Lodgepole, Middle Bakken and Three Forks). We cycled P_c under constant P_p to simulate reservoir stress changes associated with depletion and injection. The ultrasonic velocities (Vp and Vs) in the axial direction were measured along the loading path, based on which the elastic moduli and effective stress coefficient were derived. Common to all specimens, both Vp and Vs under injection are consistently higher than under depletion at the same P_c and P_p. Derived elastic moduli assuming material isotropy qualitatively agree with logging data, but are consistently higher than those based on static measurements. We found the effective stress coefficient (α) with respect to Vp and Vs is close to unity when the simple effective stress is no more than 10 MPa, regardless of wave type, lithology and loading path. α for Vp and Vs generally increases for higher simple effective stress (P_c - P_p) and beyond unity, which is contrary to the trend obtained through static deformation and against theoretical expectations. It implies that Vp and Vs become more sensitive to P_p rather than P_c as (P_c - P_p) rises. This apparent increase of α with (P_c - P_p) is *a priori* unresolved, but can be plausibly attributed to the fact that the change of (P_c - P_p) altered the rock microstructure, which essentially rendered the pore pressure more effective.

Keywords:

effective stress coefficient; ultrasonic velocity; poroelasticity; sedimentary rocks

1. INTRODUCTION

The understanding of petrophysical and geomechanical behaviors of *in situ* rock primarily relies on seismic measurements (e.g., seismic survey, acoustic logging, microseismic monitoring). The knowledge of the dependencies of rock seismic velocities on *in situ* stress and pore pressure is critical to the interpretation of subsurface attributes. Characterization of such dependencies in low-permeability and low-porosity sedimentary rocks are particularly challenging due to their inherent complex microstructures and significant anisotropy and heterogeneity, especially when complex changes in *in situ* stress and pore pressure (e.g., depletion and injection) are associated.

Laboratory experimental evidence [*Todd and Simmons*, 1972; *Christensen and Wang*, 1985; *Hornby*, 1996; *Prasad and Manghnani*, 1997; *Khaksar et al.*, 1999; *Darot and Reuschlé*, 2000; *Sarker and Batzle*, 2008] suggests that the dependencies of rock seismic velocities (V) on confining stress (P_c) and pore pressure (P_p) can be generally described with a simple function $V = f(P_c - \alpha P_p)$ where f depends on lithology and ($P_c - \alpha P_p$) is the effective stress (σ_{eff}) [*Biot*, 1962; *Nur and Byerlee*, 1971] with α being the effective stress coefficient with respect to the specific seismic wave velocity in consideration. The use of σ_{eff} [$= (P_c - \alpha P_p)$] couples the positive and negative dependencies of seismic wave velocity (V) on P_c and P_p, respectively, and α quantifies the relative contribution of P_p as compared to that of P_c. As alluded to above, the value of effective stress coefficient (α) tends to be specific to the lithology and the stressed state (P_c and P_p) the rock is subject to.

There have been a handful of rigorous theoretical derivations on effective stress coefficient for elastic moduli and velocities [e.g., *Zimmerman*, 1991; *Berryman*, 1992, 1993; *Gurevich*, 2004]. These attempts generally confirmed the aforementioned experimental findings but are mainly restricted to mono-mineralic lithologies with relatively simple microstructures. In rocks with multiple constituent minerals and complex microstructures, meaningful theoretical bounds on effective stress coefficient [*Berryman*, 1992, 1993; *Gurevich*, 2004] are offered, but its dependencies on confining stress (P_c), pore pressure (P_p) and complicated loading path remain elusive. Despite recent theoretical and experimental developments, their discrepancy still exists and awaits to be resolved. To this end, laboratory experiments are indispensable to characterize the first-order controlling factors and to verify the relevant theoretical assumptions.

In this paper, we present our experimental study on the variations of ultrasonic velocities with confining and pore pressures in six distinct lithologies from the Bakken play. Our experimental setup simulated the realistic poroelastic stress changes that occurred *in situ*. The velocities measurements were taken simultaneously with the static deformation experiments reported by *Ma and Zoback* [2016a, 2017]. We examined the similarities and differences of the effective stress coefficients and their variations between lithologies, depletion and injection scenarios, and wave types, then we offered insights on the factors that affect rocks' dynamic poroelastic response.

2. BAKKEN CORES

The cores were extracted from a vertical well in the Williston Basin, North Dakota, covering the sequences of Three Forks, Middle Bakken, and Lodgepole. Five bedding-perpendicular (vertical) and one bedding-parallel (horizontal) cores were tested in this study. Figure 1 presents the thin-section photomicrographs of the pristine cores, depicting their distinct microstructures. Table 1 summarizes the petrophysical properties of these cores.

Table 1. List of specimens and their petrophysical properties (modified from *Ma and Zoback* [2017])

Specimen Name	Rock Type[1]	Mineral Composition (wt%)			Depth (ft)	Porosity[3] (%)	Formation
		QFM[2]	Carbonates	Clays			
B1V[4]	lime-wackestone	0.08	0.87	0.05	9915.1	3.67	Lodgepole 1
B3V	fine sandstone	0.58	0.31	0.11	9967.0	7.12	Lodgepole 2
B3H[4]	fine sandstone	0.62	0.23	0.15	9967.1	7.12	Lodgepole 2
B4V	lime-packstone	0.30	0.47	0.22	10054.5	10.1	Middle Bakken 1
B9V	fine sandstone	0.70	0.19	0.10	10070.2	3.06	Middle Bakken 2
B10V	dolomite sediment	0.31	0.51	0.15	10247.9	14.35	Three Folks

Note: [1] Classification follows the recommendations by *Hallsworth and Knox* [1999].
[2] QFM: quartz, feldspar, and mica.
[3] Porosity estimated based on dry bulk density and average mineral density.
[4] V and H denote vertical and horizontal specimens.

The lithology varies significantly with depth. As shown in the compositional log (via Elemental Capture Spectroscopy (ECS)) (Figure 2b), the lithology of the Middle Bakken formation varies unpredictably between silicate-rich to carbonate-rich. The two Middle Bakken cores (B4V and B9V) represent distinct lithofacies within this sequence. As shown in Table 1, B4V contrasts B9V with significantly higher carbonate content. The lithology of the Lodgepole formation is

112 dominantly carbonitic. However, powder X-ray diffraction (XRD) analysis shows that the
113 Lodgepole core (B3V) contains more than 50% of silicates (by weight). It is possible that the
114 coring might have biased a thin layer of silicate-abundant sediment or it is likely to be a logging
115 error. The Three Forks formation, beneath the Lower Bakken, is a mixed carbonate-silicate
116 sequence, which is unambiguously represented by the specimen B10V.
117
118 The core densities were measured and compared against the logging values (Figure 2c). The
119 laboratory measurements are consistently lower than the logging values by no more than
120 0.15g/cm^3. Possible explanations for this discrepancy include liquid loss (water, oil evaporation)
121 over time and/or the core volume expansion due to stress relief upon coring. The density
122 discrepancy may affect the derivation of dynamic elastic moduli based on velocity
123 measurements, which will be discussed later.
124
125 A ternary diagram (Figure 3) is utilized to illustrate the composition of three groups of minerals:
126 (1) quartz, feldspar, and mica (QFM), (2) carbonate, and (3) clay (and kerogen). The diagram
127 suggests a sharp contrast in relative silicate and carbonate contents of the core samples, even for
128 those from the same sequence. This, together with the contrast in microstructures, is expected to
129 affect the poroelastic response of these different lithologies. Following *Ma and Zoback* [2017],
130 we divide these cores into two suites according to their mineralogy: the carbonate-rich suite
131 (B1V, B4V, and B10V, classified as lime wackstone/packstones), and the silicate-rich suite
132 (B3V, B3H, and B9V, classified as fine sandstones).
133
134 **3. METHODOLOGY**
135 Laboratory experiments were configured to subject the rock specimen under external hydrostatic
136 confining pressure (P_c) with a separately controlled internal pore pressure (P_p). The specimen
137 was put through different combinations of P_c and P_p to fully simulate the likely stress conditions
138 encountered *in situ* during depletion and injection. The experimental setup is illustrated in Figure
139 4. The test accommodates specimens of 1 inch (25.4 mm) in length and 1 inch in diameter, which
140 is housed in a servo-controlled pressure vessel. The specimen was sealed in a Viton sleeve to
141 isolate the confining fluid and then instrumented by a pair of core holders.
142

Ultrasonic velocity transducers are embedded in each core holder to emit and receive waves. The frequency of the piezoelectric crystals in use is at 1 MHz. The estimated center frequency of the measurements is around 750 kHz. The transducers are capable for *P*-wave and two mutually-perpendicular *S*-waves (*S*1 and *S*2), such that measurements of ultrasonic velocities (V_P/V_{S1}/V_{S2}) along the specimen axes are enabled. Only V_{S1} is reported (as V_S) and analyzed in this study as it was found consistently that $V_{S1} \approx V_{S2}$ in all vertical specimens. Combining all major sources of uncertainty, the error introduced in the velocity measurements is approximately 2% [*Ma and Zoback*, 2018].

We used compressed argon (Ar) gas as the pore fluid, which was regulated by one syringe pump. Argon was injected into channels built in core holders and permeated into both ends of the specimen (Figure 4). Since these Bakken cores are low in porosity and permeability, fluid saturation was facilitated by two improvements. First, we drilled three evenly-spaced but misaligned boreholes (1/3-inch depth and 1-mm diameter) on both ends of the specimen. Second, we placed porous stainless-steel disks (1/16-inch in thickness, 0.01-mm in pore size) on both ends of the specimen to evenly distribute the flow. Figure 5 illustrates the configuration of boreholes in the specimen. The effect of borehole presence on stress distribution in the specimen was considered to be inconsequential (for details, see *Ma and Zoback* [2017]).

We subjected each specimen to a maximum of 70 MPa and 60 MPa for confining pressure and pore pressure, respectively. We set the pressure ranges based on the *in situ* stress condition of the study area [*Wang and Zeng*, 2011; *Dohmen et al.*, 2014; *Yang and Zoback*, 2014] and allowed for possible stress conditions encountered during depletion and injection scenarios. The loading followed a pre-determined path to put the specimen through various possible combinations of P_c and P_p (Figure 6). The confining pressure (P_c) was loaded to maximum and then unloaded by steps of 10 MPa while maintaining pore pressure (P_p) constant. The pore pressure ranged between zero and its maximum by increments of 10 MPa. Each step of P_c and P_p was applied instantaneously, although pore pressure equilibrium within the specimen was expected to take longer. We typically waited 2-3 hours for each P_c change and at least 24 hours for P_p to ensure that the pore pressure is equilibrated. As the specimen deformation was constantly monitored, we

considered the equilibrium achieved when the time-dependent poroelastic strain reading stabilized [*Ma and Zoback*, 2017].

The specimens were prepared and tested in a room-temperature, room-dry environment and had undergone a so-called 'seasoning' procedure [*Ma and Zoback*, 2018] before testing. The seasoning cycled the specimen between zero and maximum confining stress multiple times with zero pore pressure in order to achieve reproducible measurements. The effects of the remaining fluid content on poroelasticity and experiment artefacts were discussed by *Ma and Zoback* [2018].

4. ULTRASONIC VELOCITY MEASUREMENTS

The mineralogy and microstructure varies significantly from one specimen to another. Lithological differences are expected to induce differences in the velocities and dependencies of velocities on P_c and P_p. We first summarized the dependencies of *P*- and *S*- wave velocities on P_c of all specimens to establish a general comparison. In Figure 7, the variations of ultrasonic velocities with confining pressure of all vertical specimens are displayed for a constant P_p at 10 MPa. The confining pressure (P_c) was raised from 20 MPa to 70 MPa (the maximum) and then unloaded back to 20 MPa in increments of 10 MPa to form a complete stress cycle. Common to all specimens, both *V*p and *V*s increase with P_c at a decreasing rate, although the degree of increase varies significantly between specimens. We noticed that the variations of *V*p and *V*s with P_c in the carbonate-rich specimens (B1V, B4V, and B10V) are generally moderate (less than 6%), which contrast with the greater variations in the two fine sandstones (B3V and B9V). It appears that dividing these specimens into two sub-groups according to their mineralogy also has the significance in grouping their velocity dependencies on P_c. It is worth noting that the difference in velocities between these specimens is consistent with the difference in their stiffness measured by *Ma and Zoback* [2017]. In general, greater stiffness corresponds to higher velocities (for both *P*- and *S*- waves), which is as expected. Note also there is measurable difference in *V*p and *V*s between loading and unloading, but this difference is negligible as compared to the extent of variations imposed by P_c. The loading-unloading difference is a persistent observation, which is discussed at length later in the context of depletion-injection discrepancy.

204

205 **4.1 Velocity variations along the designated loading path**

206 Figure 8 displays the response of velocity to confining stress of all six specimens under constant
207 pore pressure. The colored symbols and the associated solid fitting curves separate those constant
208 P_p data series. Data series of constant simple effective stress σ (= P_c - P_p) are linearly fitted with
209 black dashed lines, which enable the evaluation of the counteracting effects of P_c and P_p. The
210 external confining pressure P_c compacts the rock, which stiffens the rock aggregate frame and
211 causes the velocity to increase. P_p apparently acts to relieve the compaction of P_c. Along the
212 constant σ curve, the increment of P_c between adjacent data points equals to that of P_p. A vertical
213 trend is expected if P_p completely cancels out the compaction of P_c. However, the constant σ
214 curves are generally inclined, which indicates that the effects of P_p and P_c are not equivalent in
215 terms of magnitude. This suggests that the effective stress coefficient (α) is not necessarily equal
216 to unity as some theories predicate (e.g., *Gurevich* [2004]). The gradual evolution in the
217 curvature of constant P_p curves and in the inclination of constant σ curves suggests the effective
218 stress coefficient is unlikely a constant, and is dependent on both P_c and P_p. Interestingly in all
219 specimens, the slopes of constant σ curves are mostly positive for Vp but negative for Vs, albeit
220 having slight variations with the magnitude of σ. Along with the change in the inclination of
221 constant σ curves, the spacing between these curves generally decreases as σ increases. This
222 simply indicates a diminishing effect of σ magnitude on velocity increase.

223

224 Discrepancy can be found by comparing velocities between depletion and injection scenarios
225 (Figure 8). In general, velocity is higher under injection than depletion under the same (P_c, P_p)
226 condition, regardless of wave type and pressure level. The discrepancy between the two
227 scenarios is not thoroughly understood, but is generally considered to be the characteristic
228 hysteresis between loading and unloading. Notably, in specimens B3V, B3H and B4V, the slope
229 of the constant σ curves changes its sign from positive under depletion to negative under
230 injection. This implies the effective stress coefficient becomes greater than unity for the latter
231 scenario, which is counter-intuitive. We detail the derivation of effective stress coefficient with
232 respect to ultrasonic velocities in Section 6 and relevant discussion in Section 7.

233

234 It is worth noting that we did not extend the constant σ fitting curves to data points of $P_p = 0$.

This is due to the fact that a misalignment typically exists between data of P_p = 0 MPa and that of P_p = 10 MPa and above, which disrupts the constant σ trend otherwise well-fitted linearly. In most specimens, Vp (or Vs) at P_c = 20 MPa and P_p = 10 MPa is measurably higher than that at P_c = 10 MPa and P_p = 0 MPa. Considering the equal increment of P_c and P_p, it is surprising to observe such an increase of velocity. Similar observation was identified previously (e.g., by *Hornby* [1996] in a North Sea shale and by *Vasquez et al.* [2009] in some tight sandstones and medium consolidated limestones). It is unclear why the velocity change on the increase of P_p from 0 to 10 MPa along constant σ fitting curves is not consistent with that on further increase of P_p. If there is residual pore fluid present, then the lower velocity at zero P_p can be explained by the undrained response of pore pressure, which can limit the extent of velocity increase under confinement. If this is not the case, we attribute this to the fundamental difference between pore pressure and confining pressure effects on the rock's wave-propagation characteristics that is still not evident. Associated with this offset between the P_p = 0 MPa data series and the non-zero data series, the variations of velocities with confining pressure need to be described differently between them. The variations of velocities with confining pressure for zero pore pressure can be well described by the formulation below

$$V_{P/S}\Big|_{P_p} = a \cdot \exp\left(-b \cdot P_c\right) + c \tag{1}$$

where a, b, and c are fitting parameters. For velocities variations with P_c at $P_p > 0$, second-order polynomial functions are adequate.

4.2 Variations of velocities between specimens

In order to facilitate the comparison of velocities between five vertical specimens, the velocity data displayed in Figures 8 and 9 was re-arranged. In Figure 10, we compiled the constant P_p data series down to individual data points for each specimen. We followed *Ma and Zoback* [2017] to adopt the data points at P_c = 60 MPa and P_p = 30 MPa, because this stress condition is a good approximation of what is encountered *in situ*. Error bars represented the upper and lower limits of velocity variations with the changes in P_c and P_p. Notably the velocity variations with P_c and P_p are mostly insignificant in each carbonate-rich specimen as compared to the differences between specimens in the sub-group, but it is just the opposite in silicate-rich

specimens. The velocity data of these specimens generally falls into the range expected for similar lithologies under similar effective stress [*Mavko et al.*, 2009].

The compiled velocity data was plotted against specimen parameters to identify any possible relationships. In Figure 10a, the *V*p and *V*s data was first plotted against the content of clay plus kerogen, which are compliant constituents and are expected to significantly lower the overall stiffness and slow down the velocities. However, no apparent trend was identified in this relation. We suspect that how clay minerals (and kerogen) are distributed throughout the specimen is more relevant to the rock aggregate stiffness, and hence to the wave propagation velocities. The *V*p and *V*s data are also examined against porosity (Figure 10b). A clear correlation does not appear among all five vertical specimens, but we found both *V*p and *V*s decreases consistently with porosity within the carbonate-rich specimens. This is consistent with the general trend built upon a large set of carbonate rocks (summarized by *Mavko et al.* [2009]) and the trend identified in bulk modulus of these same specimens by *Ma and Zoback* [2017]. *Ma and Zoback* [2017] found these carbonate-rich specimens are generally clast-supported with pervasive and strong grain contacts. It explains why their variations of *V*p and *V*s data with P_c and P_p are not significant, but the velocities show strong dependence on porosity (and possibly on pore geometry and alignment). The silicate-rich specimens feature less persistent clastic grain contacts and tend to be occasionally disrupted by compliant components, so this plausibly explains their significant variations of *V*p and *V*s data with P_c and P_p, which may mask the effect of porosity.

5. COMPARISON OF LABORATORY MEASUREMENTS WITH SONIC LOGS

Direct comparison of velocities between laboratory measurements and sonic logs is shown in Figure 11a. Similar to Figure 10, the data points represent measurements at P_c = 60 MPa and P_p = 30 MPa and for depletion only (since its difference from injection is negligible). The laboratory measurements are generally close to the logging values. The agreement is excellent in specimen B10V (Three Forks), and the discrepancy in other specimens is within 0.5 km/s. The range of velocity variations with all applied P_c and P_p conditions (Figures 8 and 9) generally becomes insignificant when compared to the log-laboratory discrepancy. (One exception is the Middle Bakken specimen B9V, in which the range of variations in *V*p and *V*s reaches as high as

about 1 km/s and 0.5 km/s, respectively.) We generally concluded that the deviation of *in situ* stress and pore pressure from laboratory condition (P_c = 60 MPa and P_p = 30 MPa) is not a major source of this discrepancy. Interestingly, the laboratory measured *V*s is generally higher than the logging value. This is better illustrated in the *V*p vs. *V*s plot (Figure 12). The logging data cloud of each lithological unit is compared with the corresponding laboratory data points. The range of the laboratory *V*p values generally spans the range of logging data of those lithological units, however the *V*s values consistently exceed the logging data by no more than 0.4 km/s. It is unclear what caused such discrepancy. Besides the fact that the laboratory setup does not exactly replicate the *in situ* (stress, hydrous, and temperature) conditions, the sampling scale between sonic (log) and ultrasonic (laboratory) measurements might be relevant. The shear wave propagation is perhaps more sensitive to the scale difference. A generally higher laboratory *V*s value can be a result that neither the core plug nor the ultrasonic wave sampled the size of discontinuities comparable to acoustic wavelength.

Comparison between laboratory measurements and logging data is extended to dynamic elastic moduli (this is further utilized to derive a profile of the effective stress coefficient, see Appendix A). Bulk modulus (*K*) and *Young*'s modulus (*E*) are derived from *V*p and *V*s and density log by assuming stiffness isotropy:

$$K = \rho\left(V_P^2 - 4V_S^2/3\right) \tag{2}$$

$$E = \rho V_S^2\left(3V_P^2 - 4V_S^2\right)/\left(V_P^2 - V_S^2\right) \tag{3}$$

Although the discrepancy in velocities and density between logging and laboratory measurements inevitably affects the derived elastic moduli, the laboratory-derived *Young*'s moduli generally agree with the log-based values (Figure 11b). The largest difference exists in specimen B1V, which is slightly less than 15 GPa out of the log-based value of 60 GPa. The comparison of bulk modulus is generally less satisfactory (Figure 11c). Except for specimen B1V, the laboratory measurements are appreciably lower than the logging-based. In specimen B3V, the former is merely one-third of the latter. The exact reason for such discrepancy in elastic moduli is unclear. It can be partially attributed to the differences in density and velocities, but the assumption of isotropy (Eq. (2) and (3)) is also relevant. *Sone and Zoback* [2013] evaluated the

error associated with applying assumption of isotropy to inherently VTI Bossier/Haynesville shale samples and found the agreement is within 5%. The degree of deformational anisotropy of the samples used in this study generally does not exceed that of the shale samples tested by *Sone and Zoback* [2013], so the error incurred by the assumption of isotropy is of questionable significance.

6. EXPERIMENTALLY DERIVED EFFECTIVE STRESS COEFFICIENT

Formulated by *Todd and Simmons* [1972], an incremental change in seismic velocity V can be attributed to the superposition of the pore pressure (P_p) change acting around the rock constituent minerals and the pressure difference ($\sigma = P_c - P_p$) change acting on the rock aggregate.

$$dV = \left(\frac{\partial V}{\partial P_p}\right)\Big|_{\sigma} \cdot dP_p + \left(\frac{\partial V}{\partial \sigma}\right)\Big|_{P_p} \cdot d\sigma \tag{4}$$

This is analogous to the derivation of effective stress with respect to static deformation by *Nur and Byerlee* [1971] where seismic velocity V should be replaced by volumetric strain ε_v (= ε_{11} + ε_{22} + ε_{33}). In fact, seismic velocity V in Eq.(4) can be generalized for a handful of physical quantities (represented by Q). Rearranging Eq.(4), the formulations of the effective stress (σ_{eff}) and the effective stress coefficient (α) becomes self-explanatory:

$$dQ = \left(\frac{\partial Q}{\partial \sigma}\right)\Big|_{P_p} \cdot \left\{dP_c - \alpha \cdot dP_p\right\} \tag{4a}$$

$$\alpha = 1 - \left(\frac{\partial Q}{\partial P_p}\right)\Big|_{\sigma} \Big/ \left(\frac{\partial Q}{\partial \sigma}\right)\Big|_{P_p} \tag{4b}$$

Eq.(4b) had been employed previously to derive the effective stress coefficient with respect to experimentally measured seismic velocities [*Todd and Simmons*, 1972; *Christensen and Wang*, 1985; *Hornby*, 1996; *Prasad and Manghnani*, 1997; *Sarker and Batzle*, 2008] and volumetric strain [*Warpinski and Teufel*, 1992; *Ojala and Sønstebø*, 2010; *Ma and Zoback*, 2017; *Ma*, 2019].

Todd and Simmons [1972] originally noted that Eq.(4) is based on the assumptions that the rock constituent minerals are perfectly elastic and the pore pressure uniformly acts on each mineral

353 grain. However, the utilization of Eq.(4b) to derive the effective stress coefficient does not
354 always require such assumptions. Close examination of Eq.(4b) reveals that the denominator and
355 numerator of the second term, i.e., $\partial Q/\partial P_p|_\sigma$ and $\partial Q/\partial \sigma|_{Pp}$, represent the contribution of pressure
356 difference (P_c - P_p) and P_c to the change in a physical quantity. Therefore, the effective stress
357 coefficient, which quantifies the pore pressure effect, is obtained by subtracting this ratio
358 between the two from unity. Eq.(4b), as consistent with the concept of effective stress
359 (coefficient), is strictly applicable to most scenarios without being affixed to many assumptions
360 originally associated with Eq.(4). As we noted elsewhere in this paper, the tested rock specimens
361 (and probably some of their constituent mineral grains such as compliant clays and organic
362 matter) are not perfectly elastic, and some structural alteration or damage with loading cycles is
363 possible. We employed Eq.(4b) purely as an *ad hoc* approach to derive the effective stress
364 coefficient with respect to measured seismic velocities (V_P and V_S). This practice is also
365 convenient in view of our experimental program and consistent with the concurrent work on
366 static deformation reported by *Ma and Zoback* [2017].
367
368 Figure 13 displays the variations of effective stress coefficient α (with respect to ultrasonic
369 velocities) with simple effective stress (σ) for constant P_p. When σ is at its minimum (= 10 MPa),
370 α is close to unity, regardless of lithology, loading path, and pore pressure level. As σ increases,
371 α consistently increases for all pore pressure levels. The only exceptions are B9V and B10V
372 under depletion where no systematic variations were observed. The extent of α increase with σ is
373 distinct from specimen to specimen, and between compressional and shear waves. For example
374 in specimen B1V, α (with respect to Vp under depletion) gradually increases from ~0.85 at σ =
375 10 MPa to ~1.05 at σ = 60 MPa; while in B4V, α increases from ~0.95 at σ = 10 MPa to nearly
376 2.25 at σ = 60 MPa. Again in specimen B1V, α (with respect to V_S under depletion) hardly
377 deviates from unity but α (with respect to V_P under depletion) unequivocally rises with σ, though
378 the latter was generally lower. This suggests that the mechanism for effective stress changes with
379 wave type (further discussed in Section 7.1). Nonetheless, it is worth noting that the derivation of
380 the effective stress coefficient at high σ is subject to significant uncertainty. Since the calculation
381 of α is based on the curve-fitting to constant σ and P_p trends, the corresponding data series only
382 have limited data points at high σ. Therefore, the derived variations of effective stress coefficient
383 with σ when σ exceeds 40 MPa have questionable significance.

Notably, in almost all specimens the variations of α with σ for all constant P_p levels nearly coincide. This suggests that the pore pressure's absolute magnitude has only negligible control on α, but the magnitude of σ is important. The rise of α with σ signifies that the effect of pore pressure on counteracting P_c-induced compaction is augmented. This trend with respect to velocities is diametrically opposite to what was identified from the static deformation data in the same specimens [*Ma and Zoback*, 2017], in which the rise of either σ or P_p causes α to decrease. This is not unreasonable since σ can effectively alter the rock microstructure through compaction and may result in different impacts on dynamic and static characteristics. However, this could also be an experimental artifact, considering the complexity of high-frequency wave propagation. Relevant discussion can be found in Section 7.1 and 7.2.

Differences of the effective stress coefficient α exist between depletion and injection. The coefficient α is generally higher during injection than during depletion given the same σ and P_p. This is consistent with the static data by *Ma and Zoback* [2017]. In certain specimens during depletion (e.g., B1V and B9V), the variations of the effective stress coefficient appear to be erratic, however in all specimens during injection, the increase of α with σ is monotonic, and appears to be more systematic than under depletion. The fact that deformation associated with injection (unloading confinement) is mostly elastic is perhaps relevant. Additional discussion on depletion-injection difference is offered in Section 7.3.

7. DISCUSSION

In this section, we provide additional thoughts on the experimentally-derived effective stress coefficients and how it is related to the poroelastic behavior of the tested Bakken cores. We focus on the following experimental observations: (1) effective stress coefficient with respect to seismic velocities is larger than unity; (2) effective stress coefficient with respect to seismic velocities is larger than that to volumetric deformation, and the coefficient to V_s is generally higher than that to V_p and in slightly different trend; and (3) discrepancy of effective stress coefficient with respect to the same physical quantity exists between injection and depletion. The apparent variations of the effective stress coefficient with P_c and P_p help understand the rock microstructure and its likely alterations in relation to changes in P_c and P_p.

415

416 **7.1 Effective stress coefficient beyond unity**

417 It is particularly intriguing that the effective stress coefficients with respect to ultrasonic V_P and
418 V_S in some specimens increase appreciably with σ beyond unity (Figure 13). These cases imply
419 that the pore fluid effect augments with increasing σ and becomes more effective than confining
420 pressure. This does not significantly affect the calculated values of σ_{eff} since the effective stress
421 coefficient deviates much from unity only when P_p is substantially lower than P_c. However this
422 observation is rather surprising as normally we expect the opposite, which has been identified in
423 a handful of sedimentary rocks [*Todd and Simmons*, 1972; *Christensen and Wang*, 1985;
424 *Hornby*, 1996; *Prasad and Manghnani*, 1997; *Sarker and Batzle*, 2008] and observed in the
425 effective stress coefficient with respect to volumetric deformation we measured simultaneously
426 in the same rock specimens [*Ma and Zoback*, 2017]. Admittedly it is difficult to compare the
427 effective stress coefficients with respect to different rocks and different physical quantities as the
428 underlying mechanism differs from one to another. Nonetheless this intriguing phenomenon may
429 offer insights to the possible influence of experimental artifacts/limitations and complex fluid-
430 rock interaction. Specifically, we offer several explanations to this phenomenon, mainly in terms
431 of pore pressure inequilibrium when high-frequency wave passes through and the microstructure
432 alteration/damage under stress. These issues are considered interconnected and detailed as
433 follows.

434

435 ***7.1.1 Pore pressure inequilibrium***

436 *Gassmann*'s [1951] fluid substitution is based on the assumption that the pore pressure within the
437 pore space remains equilibrated when elastic waves propagate through the rock. However, this is
438 the idealized case since the elastic deformation of the rock within the short duration of high-
439 frequency waves passing may induce incomplete pore pressure equilibrium, especially in
440 elongated cracks. This transient undrained condition stiffens the rock, which results in higher
441 velocity than the low-frequency or static case. This, however, requires the understanding of the
442 crack types and crack density throughout the rock matrix, and the closure of cracks under
443 confinement.

444

445 The deviation of the effective stress coefficient from unity can also be understood in terms of the
446 variation of fluid bulk modulus with pore pressure [*Batzle and Wang*, 1992]. Similar to other
447 gases, Argon is considered a soft-fluid when pore pressure is low, but its bulk modulus
448 apparently increases, considering the pressure range we applied (0-60 MPa). The relation
449 between fluid stiffness and crack stiffness is critical as it dictates whether the saturated rock is
450 pore-supported or fluid-supported [*Mavko and Jizba*, 1991]. Nonetheless, both the undrained
451 pore pressure inequilibrium and the fluid bulk modulus stiffening are likely to induce an
452 unrelaxed or stiffer rock [*Mavko and Vanorio*, 2010; *Adam and Otheim*, 2013], namely an
453 exaggerated pore pressure effect (lower effective stress coefficient than unity), which cannot
454 explain why effective stress coefficient went beyond unity and increases with σ.
455
456 ***7.1.2 Dual-porosity media***
457 The variations of effective stress coefficient with P_p and P_c can also be analyzed in the context of
458 dual-porosity, dual-permeability media [*Warrent and Root*, 1963; *Berryman and Wang*, 1995,
459 2000; *Berryman and Pride*, 2002]. Typically the specimen at the core scale is considered to be
460 representative of intact rock (porous matrix), however due to various reasons (damage associated
461 with coring and handling, stress-relaxation and desiccation) the core specimen can contain
462 numerous fractures that intersect the porous matrix. Such an example is shown in Figure 15 for
463 specimen B1V.
464
465 Fracture deformation in a dual-porosity system introduces issues of pore pressure inequilibrium
466 and rock microstructure alteration. Suggested by *Berryman and Wang* [2000], fractures have two
467 very important effects on the core wave propagation properties. One is that the presence of
468 fractures softens the rock frame, which depends on the fracture compliance; the other is that the
469 fractures constitute a high-permeability pathway for fluid flow, which contrasts the low-
470 permeability rock porous matrix. In much longer time scales such as reservoir depletion or
471 equivalent static deformation experiments, the dual-porosity media can effectively behave like a
472 single-porosity media when pressure between the porous matrix and the fractures eventually
473 equilibrate. However, in much shorter time scales such as the high-frequency seismic wave
474 propagation, the contrast of permeability between porous matrix and the fractures can partially
475 contribute to the pore pressure anomaly inside the matrix as discussed in the last section. This

476 pore pressure anomaly is analogous to the inequilibrium inside the elongated micro-pore space
477 due to squirt flow, but at larger scales.
478
479 What separates dual-porosity and single-porosity media is the fracture property, which is
480 dependent on the confining pressure and the pore pressure within the fractures. The fracture
481 deformation with stress changes the rock framework stiffness, which results in the change in the
482 poroelastic behavior. As the permeability of fractures changes with its deformation, the transient
483 poroelastic behavior during wave propagation will be further impacted. The two effects of
484 fractures are inter-dependent and expected to be non-linear with the confining pressure and pore
485 pressure. It is plausible that under the same simple effective stress, the structure of the dual-
486 porosity media slightly varies with pore pressure magnitude, which in some circumstances may
487 yield variations of the effective stress coefficient beyond unity.
488
489 ***7.1.3 Anisotropy, in situ stress anisotropy and damage***
490 It is important to note that in our experiments we confined the cores under hydrostatic stress
491 conditions ($S_1 = S_2 = S_3 > P_p$) to the mean stress magnitudes comparable to the inferred *in situ*
492 conditions. As discussed by *Ma and Zoback* [2017], this is not fully representative of the three-
493 dimensional stress conditions the rocks actually experienced *in situ* (c.f., *Ma and Haimson*
494 [2016]. This results in the core specimen along the direction of *in situ* least principal stress (S_3)
495 (presumably along one of the lateral directions for bedding-perpendicular cores) being loaded to
496 the magnitude that exceeds *in situ* values. Since these sedimentary rocks are typically anisotropic
497 (mostly VTI, vertical transversely isotropic) in deformability and strength, the hydrostatic
498 loading might have introduced excessive compaction along core axis where the *in situ* least
499 principal stress (S_3) was prevailing while deficit compaction in other directions. The contrast in
500 mechanical properties between principal directions, in conjunction of inherent rock
501 heterogeneity, is likely to induce tensile stresses, which may cause irreversible deformation, or
502 damage within the rock. The damage can also be promoted by the tensile loading by pore
503 pressure. Over the course of multiple loading cycles, it is possible that the rock might undergo
504 progressive damage, in forms of microcracks extension or compliance component permanent
505 compaction. This again tends to promote pore fluid infiltration and saturation, further damages

506 the rock. These can possibly explain the increase of effective stress coefficient with pore
507 pressure under constant σ and its value exceeds unity.
508
509 ***7.1.4 Microstructure alteration and grain surface interactions***
510 Another factor that affects the effective stress coefficient is the possible microstructure alteration
511 under confining pressure and pore pressure loading, even when any damage is absent. This
512 involves the surface interaction between grain contacts. *Christensen and Wang* [1986] found in
513 Berea sandstone that the effective stress coefficient for V_S, is slightly beyond unity but not for
514 V_P, and they attributed it to the deformation of highly compressible clay cement between stiff
515 quartz grains. Utilizing the idea of normal and tangential contact stiffness introduced by *Digby*
516 [1981], *Christensen and Wang* [1986] argued that the increase of pore pressure compresses the
517 clay cement that coats the clastic grains and fill the pore space adjacent to the grain contacts. The
518 volume of the clay cement and how they bridge the clastic grain contact is critical for elastic
519 wave propagation. Fulfilling certain conditions, the equal increments of confining pressure and
520 pore pressure can induce the increase of normal contact stiffness (V_P) but the decrease of
521 tangential contact stiffness (V_S). The experimental observations by *Christensen and Wang* [1986]
522 for V_S is consistent with what we observed in this study, and especially in that the effective stress
523 coefficient for it further increases with the simple effective stress. However, our observations for
524 V_P are different from theirs. The clay coatings in Berea sandstone are relatively thin so that it
525 ultimately gets highly compressed between clastic grains under reasonable confinement, while
526 this is not necessarily the case in these Bakken rocks. Examples are shown in Figure 16. Under
527 certain conditions, equal increments of confining pressure and pore pressure might produce a net
528 decrease in both normal and tangential stiffness of the grain contact, which essentially causes the
529 effective stress coefficient for both V_P and V_S to exceed unity and to increase with simple
530 effective stress. A schematic diagram is provided in Figure 17 to illustrate this. Under low simple
531 effective stress, because the clastic grain contacts are not fully established, either the decrease of
532 P_C or the increase of P_P by the same increment will result in approximately equal effects on the
533 contact stiffness, i.e., α is close to unity. Under high simple effective stress, the effect produced
534 by the increase of P_P is likely to compress much of the clay minerals adjacent to clastic grains,
535 affecting the contact stiffness more effectively than the decrease of P_C by the same amount. Built
536 on this hypothetical model, we detail in Appendix B on conditions that need to be fulfilled

following *Digby* [1981] and *Christensen and Wang* [1986]. This is likely to be further impacted by the presence of any microcracks surrounding the clastic grains (e.g., Figure 16), which is difficult to reason quantitatively. *Elata and Dvorkin* [1996] explored the mechanical contact interaction between cemented clastic grains via analytical solutions. They found the contrast of stiffness between cement material and the clastic grain, the grain radius and the cement thickness significantly affect the rock aggregate stiffness. Their model is illuminating in the context of our observations.

7.2 Effective stress coefficient with respect to different physical quantities

We noticed the derived effective stress coefficient for seismic velocities in this study is different between V_P and V_S, and neither is the same with that for volumetric strain in the same specimens and subject to the same experimental program [*Ma and Zoback*, 2017]. This discrepancy is not surprising since different physical quantities involve different physical mechanisms, even in the same rock specimen [*Berryman*, 1992]. It has long been observed that the effective stress coefficients with respect to different physical quantities vary significantly. *Warpinski and Teufel* [1992] showed in several sedimentary rocks that the effective stress coefficient for volumetric deformation is different from that for permeability. *Zoback and Byerlee* [1975] showed in Berea sandstone that the effective stress coefficient for permeability is generally larger than unity while in volumetric compression tests (e.g., *Hart and Wang* [1995] it never exceeds unity. Apparently, the mechanism of fluid transport might differ significantly from that of volumetric deformation. *Zoback and Byerlee* [1975] suggested that considerable deformation of pore-lining clays with pore pressure enhances the permeability but its effect on the rock skeleton deformation is negligible. This urges us to identify different rock constituents as they deform differently under the loading of external confinement and pore pressure. It is also consistent with our argument regarding grain surface interactions in Section 7.1.

Our tests in these Bakken cores are among the few that directly compare the effective stress coefficient between dynamic (seismic velocities) and static (volumetric strain) quantities. In general, effective stress coefficient for seismic velocities is larger than the latter, regardless of the apparent variations with stress and pore pressure. Fundamentally both seismic velocities and static compression deform the rock volumetrically, but unlikely at the same magnitude. The

amount of deformation (in form of vibration) caused by wave propagation through the rock is a few orders smaller than the strain produced by the static loading (c.f., *Mavko et al.* [2009]. In addition, dynamic strain associated with the high-frequency wave is considered to be primarily elastic, which is unlikely to induce inelastic deformation (e.g., compliant component compaction or microcrack closure). Recent studies on concurrent dynamic and static measurements in sedimentary rocks also confirmed the fundamental differences between the two physical quantities and their sensitivities to stresses [*Fjær*, 2009; *Sone and Zoback*, 2013; *Meléndez-Martínez and Schmitt*, 2016; *Ong et al.*, 2016]. The time scale of deformation is also important. As discussed earlier, high-frequency seismic vibration typically involves the velocity anomaly due to pore pressure inequilibrium. Such artifact is mostly absent in static tests over much longer time period.

Another issue is associated with the specimen anisotropy. The reported velocities in this study are consistently along the specimens' axes. These specimens are typically considered as VTI materials and we expect significantly different response between bedding-perpendicular and bedding-parallel directions. Comparison of the seismic velocities between two orthogonally aligned specimens (B3V and B3H) in Figures 8 and 9 shows that velocities along the beddings are generally higher than those perpendicular to the beddings. The different response is generally attributed to the alignment of compliant components (such as pores, organic matters, microcracks, porous clay minerals). Although the seismic wave-induced vibration is also volumetric, it is sensitive to the traveling direction. In this sense, we also expect the dynamic effective stress coefficient to be different from that derived from the static volumetric deformation tests by *Ma and Zoback* [2016b, 2017].

7.3 Difference between depletion and injection

The fact that effective stress coefficient is generally higher during injection than during depletion and its variation is more systematic given the same σ and P_p is quite intriguing. *Ma and Zoback* [2017] made similar observations in static measurements, and they attributed it to certain experimental artifacts (e.g., pore pressure inequilibrium) and processes that actually altered the microstructure of the rock. In Section 7.1, these same factors have been discussed regarding that

598 the effective stress coefficient increases beyond unity. Simply, the effects of these factors are
599 also relevant to the depletion-injection discrepancy. We briefly discuss them here.
600
601 Since depletion and injection scenarios in this study were simply simulated by loading and
602 unloading confining pressure when pore pressure was held constant, the microstructure change in
603 the rock is largely a result of loading-unloading hysteresis. In these Bakken specimens, the
604 deformation upon loading typically involves microcrack closure and compliant component
605 compaction [*Ma and Zoback*, 2017]. Although unloading is generally considered elastic,
606 deformation induced by loading may not be fully reversible. In the event that the pore
607 connectivity is highly sensitive to grain contact and microcrack/compliant component
608 deformation, the contrast between inelastic loading and elastic unloading can explain why the
609 variations of the effective stress coefficient during injection is more systematic than during
610 depletion and why the later is generally larger. Similar observations have been noted previously
611 by *Bernabé* [1986] and *Warpinski and Teufel* [1992] in their experiments. *Ma and Zoback* [2017]
612 discussed the interaction between static loading/unloading and the pore fluid penetration and the
613 likely influences on the effective stress coefficient. However, this is highly variable from
614 specimen to specimen.
615
616 The rock microstructure variation between loading (depletion) and unloading (injection) further
617 affects the ultrasonic wave propagation. What is relevant is the deformation of (1) fractures and
618 (2) microcracks/pores. The fracture deformation between depletion and injection mainly affects
619 the effective dual-porosity system, while microcracks/pores deformation specifically affects the
620 local squirt flow. As discussed in Section 7.1, both are associated with the pore-pressure
621 inequilibrium caused by undrained behavior when high-frequency wave propagates. Since we
622 only expect partial recovery of deformation induced by loading (depletion) upon unloading
623 (injection), the aspect-ratio of fractures/microcracks can be generally higher during injection,
624 which may promote this pore pressure artifact.
625
626 **8. CONCLUDING REMARKS**
627 We performed a suite of hydrostatic compression experiments in six Argon-saturated Bakken
628 cores to characterize their dynamic poroelastic response to confining and pore pressures. We

cycled the confining pressure under constant pore pressures to simulate the scenarios of depletion and injection. The ultrasonic *V*p and *V*s in the axial direction were measured and the corresponding elastic moduli and effective stress coefficient were derived.

As expected, both *V*p and *V*s in all specimens consistently increase with confining pressure for constant pore pressure and decrease with pore pressure for constant confinement. At the same confining and pore pressure, both *V*p and *V*s under injection are consistently higher than under depletion. Elastic moduli were calculated based on the velocities by assuming isotropy. The experimentally measured velocities and the calculated elastic moduli were compared with the logging-derived values, which yields qualitative agreement.

Based on the variations of velocities with respect to confining pressure and pore pressure, we derived the corresponding effective stress coefficient (α). We found α is close to unity when the simple effective stress is no more than 10 MPa, regardless of wave type, lithology and loading path. The effective stress coefficient typically increases for higher simple effective stress, which is contrary to the trend obtained through static deformation by *Ma and Zoback* [2017] and against theoretical expectations. It implies that the pore pressure effect strengthens with increasing simple effective stress and becomes more significant than the effect of confining pressure in these cases. The reason for this apparent increase of α with the simple effective stress is *a priori* unclear, but can be plausibly attributed to the experimental artifacts such as pore pressure inequilibrium and cyclic loading and pore fluid induced progressive damage, which altered the rock microstructure and essentially rendered the pore pressure more effective.

Despite possible experimental artifacts, the variations of velocities and the corresponding α with pressure highly differ from specimen to specimen. No apparent correlation has been identified with respect to lithology or porosity. However we generally attribute distinct poroelastic characteristics between specimens to the abundance of compliant component and how it is distributed throughout the rock matrix. Future study of the dynamic poroelastic behaviors of tight rocks focusing on the deformation of different constituents is desired to fully understand the underlying mechanism.

ACKNOWLEDGEMENT

This work was supported by funding from the Stanford Rock Physics and Borehole Geophysics Project (SRB). The Bakken cores used in this study were kindly furnished by the Hess Corporation. Experimental data is available from the corresponding author upon request.

REFERENCES

Adam, L., and T. Otheim (2013), Elastic laboratory measurements and modeling of saturated basalts, J. Geophys. Res. Solid Earth, 118, 840–851, doi:10.1002/jgrb.50090.

Batzle, M., and Z. Wang (1992), Seismic properties of pore fluids, *Geophysics*, 57, 1396–1408.

Bernabé, Y. (1986), The effective pressure law for permeability in Chelmsford granite and Barre granite, *Int. J. Rock Mech. Min. Sci.* 23(3), 267-275.

Berryman, J.G. (1992), Effective stress for transport properties of inhomogeneous porous rock: *J. Geophys. Res.*, 97, 17409–17424.

Berryman, J.G. (1993), Effective stress rules for pore-fluid transport in rocks containing two minerals, *International Journal of Rock Mechanics and Mining Sciences & Geomechanics Abstracts*, 30,1165–1168.

Berryman, J.G. and H. F. Wang (1995), The elastic coefficients of double-porosity models for fluid transport in jointed rock, *J. Geophys. Res.*, 100 (B12), 24611-24627.

Berryman, J.G. and H. F. Wang (2000), Elastic wave propagation and attenuation in a double-porosity dual-permeability medium, *International Journal of Rock Mechanics and Mining Sciences*, 37,63-78.

Berryman, J.G. and S. R. Pride (2002), Models for computing geomechanical constants of double-porosity materials from the constituents' properties, *J. Geophys. Res.*, 107 (B3), 2052.

Biot, M.A. (1962), Mechanics of deformation and acoustic propagation in porous media, *Journal of Acoustic Society of America* 28: 168-191.

Christensen, N.I. and H. F. Wang (1985), The influence of pore pressure and confining pressure on dynamic elastic properties of Berea sandstone, *Geophysics* 50(2): 207-213.

Darot, M. and T. Reuschlé (2000), Acoustic wave velocity and permeability evolution during pressure cycles on a thermally cracked granite, *International Journal of Rock Mechanics and Mining Sciences* 37: 1019-1026.

Digby, P. J. (1981), The effective elastic moduli of porous granular rocks, *J. Appl. Mech.* 48: 803-808.

Dohmen, T., J.-P. Blangy, and J. Zhang (2014), Microseismic depletion delineation, *Interpretation* 2, SG1-13.

694 Elata, D. and J. Dvorkin (1996), Pressure sensitivity of cemented granular materials, *Mechanics*
695 *of Materials* 23: 147-154.
696 Gassmann, F. (1951), Über die elastizität poröser medien, Vierteljahrsschrift der
697 Naturforschenden Gesellschaft in Zürich, 96, 1–23.
698 Gurevich, B., (2004), A simple derivation of the effective stress coefficient for seismic velocities
699 in porous rocks, *Geophysics*, 69(2), 393–397.
700 Hallsworth C.R. and RWO.'B. Knox (1999), BGS Rock Classification Scheme, Volume 3,
701 Classification of sediments and sedimentary rocks. British Geological Survey Research
702 Report, RR 99-03.
703 Hart, D. J. and H. F. Wang (1995), Laboratory measurements of a complete set of poroelastic
704 moduli for Berea sandstone and Indiana limestone, *J. Geophys. Res.*, 100(B9), 17741–
705 17751.
706 Hornby, B.E. (1996), An experimental investigation of effective stress principles for sedimentary
707 rocks: SEG 1996 annual meeting.
708 Mavko, G. and D. Jizba (1991), Estimating grain-scale fluid effects on velocity dispersion in
709 rocks, *Geophysics* 56(12): 1940-1949.
710 Khaksar, A., C. Griffiths, and C. McCann (1999), Effective stress coefficient for P- and S-wave
711 velocity and quality factor in sandstone, example from Cooper basin, Australia: 69th Annual
712 International Meeting, SEG, Expanded Abstracts, 192–195.
713 Mavko G., T. Mukerji, and J. Dvorkin (2009), The rock physics handbook: Tools for seismic
714 analysis of porous media, 2nd Ed. Cambridge University Press.
715 Mavko G. and T. Vanorio (2010), The influence of pore fluids and frequency on apparent
716 effective stress behavior of seismic velocities, *Geophysics* 75(1), N1-N7.
717 Ma, X. and B. Haimson (2016), Failure characteristics of two porous sandstones subjected to true
718 triaxial stresses, *J. Geophys. Res. Solid Earth.*, doi: 10.1002/2016JB012979.
719 Ma, X. and Zoback, M. (2016a), Laboratory investigation on effective stress in Middle Bakken:
720 implications on poroelastic stress changes due to depletion and injection. 50th U.S. Rock
721 Mechanics Geomechanics Symposium, Houston, TX, June 26-29, 2016.
722 Ma, X. and M. Zoback (2016b) Experimental study of dynamic effective stress coefficient for
723 ultrasonic velocities of Bakken cores. SEG Technical Program Expanded Abstracts 2016: pp.
724 3221-3225. doi: 10.1190/segam2016-13607443.1.
725 Ma, X. and Zoback, M. (2017), Laboratory experiments simulating poroelastic stress changes
726 associated with depletion and injection in low-porosity sedimentary rocks, *Journal of*
727 *Geophysical Research-Solid Earth* 122 (4): 2478-2503, doi:10.1002/2016JB013668.

728 Ma, X. and Zoback, M. (2018), Static and dynamic response of Bakken cores to cyclic
729 hydrostatic loading, *Rock Mechanics and Rock Engineering*, doi:10.1007/s00603-018-1443-
730 z.
731 Ma, X. (2019), Volumetric deformation, ultrasonic velocities and effective stress coefficients of
732 St Peter sandstone during poroelastic stress changes, *Rock Mechanics and Rock Engineering*.
733 doi:10.1007/s00603-019-01750-7.
734 Meléndez-Martínez, J. and D.R. Schmitt (2016). A comparative study of the anisotropic dynamic
735 and static elastic moduli of unconventional reservoir shales: Implication for geomechanical
736 investigations. Geophysics, 81(3), D245-D261.doi: 10.1190/geo2015-0427.1.
737 Nur, A. and J. Byerlee (1971), An exact effective stress law for elastic deformation of rock with
738 fluids, *Journal of Geophysical Research* 76, 6414-6419.
739 Ojala, I.O. and E.F. Sønstebø (2010), The effective stress coefficient in Pierre shale, AAPG
740 Hedberg Conference, Austin, Texas.
741 Ong, O. N., Schmitt, D. R., Kofman, R. S. and Haug, K. (2016), Static and dynamic pressure
742 sensitivity anisotropy of a calcareous shale. *Geophysical Prospecting*, 64: 875–897.
743 doi:10.1111/1365-2478.12403
744 Prasad, M., and M.H. Manghnani (1997), Effects of pore and differential pressure on
745 compressional wave velocity and quality factor in Berea and Michigan Sandstones:
746 *Geophysics* 62, 1163–1176.
747 Sarker, R. and M. L. Batzle (2008), Effect stress coefficient for North Sea shale – An
748 experimental study: SEG 2008 Annual meeting.
749 Todd, T. and G. Simmons (1972), Effect of pore pressure on the velocity of compressional
750 waves in low-porosity rocks, *Journal of Geophysical Research* 77, 3731-3743.
751 Wang, C. and Zeng, Z., 2011, Overview of geomechanical properties of Bakken formation in
752 Williston Basin, North Dakota: 45th US Rock Mechanics / Geomechanics Symposium held
753 in San Francisco, CA, June 26–29, 2011.
754 Warpinski, N.R. and L.W. Teufel (1992), Determination of the effective stress law for
755 permeability and deformation in low-permeability rocks: *SPE Formation Evaluation*.
756 No.20572, 123-131.
757 Warren, J. E., and Root, P. J. (1963), The behavior of naturally fractured reservoirs, *Soc. Pet.*
758 *Eng. J.*, 3, 245–255.
759 Winkler, K. W. (1983), Contact stiffness in granular porous materials: comparison between
760 theory and experiment, *Geophys. Res. Lett.*, 10, 1073-1076.
761 Yang, Y. and M. D. Zoback (2014), The role of preexisting fractures and faults during multistage
762 hydraulic fracturing in the Bakken formation, *Interpretation*, 2, SG25-39.
763 Zimmerman, R.W. (1991), Compressibility of sandstones, Elsevier. *pp*.172.

764 Zoback, M.D., and J.D. Byerlee (1975), Permeability and effective stress, *AAPG Bull.*, 59,154-
765 158.
766
767

Appendix A. Static-dynamic moduli correlation and effective stress coefficient profile

Here we discuss the relationship between static and dynamic elastic moduli and its application to deriving a continuous effective stress coefficient. First, we compare the static bulk modulus derived from hydrostatic compression tests by *Ma and Zoback* [2017] with the dynamic bulk modulus derived from ultrasonic velocity measurements in this study. It is shown in Figure A1a and both data sets were taken at P_c = 60 MPa and P_p = 30 MPa during depletion (the injection-depletion discrepancy is negligible in this comparison). It is evident that K_{bulk} derived from ultrasonic velocities (via Eq. (3)) is generally larger than the static values. On average, the former is around 1.3 times of the latter for each specimen. For this reason, the effective stress coefficient calculated from dynamic K_{bulk} is consistently smaller than the static one (Figure A1a). According to *Nur and Byerlee* [1971], the effective stress coefficient α is obtained by

$$\alpha = 1 - K_{bulk}/K_{grain} \quad \text{(A1)}$$

where K_{grain} is the constituent minerals. K_{grain} can be inferred based on rock mineral composition, but it is theoretically difficult for rocks composed of multiple minerals. For convenience, we used the Voigt mixing average to obtain the upper bound of K_{grain} as the input for Eq. (A1). For this reason, the effective stress coefficient calculated from dynamic K_{bulk} is consistently smaller than the static one (shown in Figure A1b). The discrepancy between static and dynamic elastic moduli is a common observation (e.g., *Sone and Zoback* [2013]). It can be attributed to the fact that static measurement may include certain amount of inelastic deformation, while the wave propagation-induced deformation (dynamic) is considerably smaller and likely be elastic. An elaborate discussion on this issue was made by *Sone and Zoback* [2013].

The dynamic-static moduli relationship facilitates the extrapolation from one to the other. Since the acoustic velocities are often measured by the logs, a continuous profile of static parameters can be obtained utilizing this correlation. The same procedure using Eq. (6) can be applied to derive the static effective stress coefficient from the sonic logging data. We utilized the acoustic log and density log (Figure 2) to estimate K_{bulk} and compositional log for K_{grain}. Since consistent discrepancy between static K_{bulk} and dynamic K_{bulk} exists (by a ratio of approximately 1.3 as noted above), we investigated the possibility of inferring the static K_{bulk} from dynamic K_{bulk} by normalizing the latter by this *ad hoc* ratio of 1.3. After normalization, the log-based profile of

799 effective stress coefficient is computed (Figure 11d) and compared with the static data from *Ma*
800 *and Zoback* [2017]. The comparison is promising, although in specimens B1V and B3V, the
801 laboratory values of the rest of specimens are considerably lower than the log-based. It is worth
802 noting that the derivation of effective stress coefficient presented in Section 6 is strictly
803 applicable to characterizing the variations of effective stress coefficient with confining pressure
804 and pore pressure within single core specimen under the designed experimental program. It is not
805 practical in deriving a continuous profile of effective stress as shown above in applications such
806 as pore pressure prediction and frac gradient calculation.
807
808 **Appendix B. Effective stress coefficient in relation to grain contact stiffness**
809 The increase of the effective stress coefficients for both *V*p and *V*s with simple effective stress
810 requires the decrease of rock normal and shear stiffness. Here we follow the model by
811 *Christensen and Wang* [1986] to derive the conditions that allow for this observation.
812 Conceptually the rocks are composed of spherical clastic grains, which are coated by or
813 embedded in compliant components (e.g., clay minerals). The stiffness of the rock largely
814 depends on the clastic grains contact. The normal and tangential contact stiffness (D_n and D_t), an
815 idea introduced by *Digby* [1981] and *Winkler* [1983], are affected by the external confining
816 stress and the internal pore pressure. D_n and D_t increases with confining pressure since it forces
817 adjacent clastic grains together and compresses the compliant components in between. D_n and D_t
818 shall principally decrease with pore pressure, but the effect of compression of compliant
819 components by pore pressure on stiffness is complicated. *Winkler* [1983] gave the relationship
820 between velocities and D_n and D_t:

821 $$V_P^2 = \frac{C}{20\pi R\rho}\left(3D_n + 2D_t\right) \tag{B1}$$

822 $$V_S^2 = \frac{C}{20\pi R\rho}\left(D_n + \frac{3}{2}D_t\right) \tag{B2}$$

823
824 where parameter C depends on the average number of contacts per grain. R and ρ are the grain
825 radius and grain density, respectively.
826

827 Apparently, the changes of D_n and D_t in response to equal increments of P_c and P_p dictate the
828 changes of Vp and Vs. When the change of the terms $(3D_n + 2D_t)$ or $(D_n + 3D_t/2)$ is positive, the
829 corresponding effective stress coefficient is less than unity, and when negative, the coefficient
830 becomes greater than unity. In some specimens we found the coefficients for both Vp and Vs are
831 beyond unity. Specifically, the following conditions should be satisfied
832
833 $$d\left(3D_n + 2D_t\right) < 0 \tag{B3}$$
834 $$d\left(D_n + \frac{3}{2}D_t\right) < 0 \tag{B4}$$
835 or simply
836 $$\frac{\Delta D_t}{\Delta D_n} < -\frac{3}{2} \tag{B5}$$
837
838 The condition prescribed by Eq.(B5) requires that magnitude of $dD_t/d\sigma$ is at least 1.5 times that
839 of $dD_n/d\sigma$. In other words, the weakening of the tangential contact stiffness D_t by pore pressure is
840 relatively more than the strengthening of the normal contact stiffness D_n by confining pressure.
841 The model utilizing the contact stiffness theoretically predicts the effectiveness of pore pressure
842 as compared to confining pressure, but the variations of effective stress coefficients (α) with σ
843 are not *a priori* straightforward. It is expected that $dD_n/d\sigma$ under high σ becomes smaller than
844 under low σ due to the establishment of the grain-to-grain contact. However $dD_t/d\sigma$ is not
845 proportionally changing since it is also dependent on the compressibility of the compliant
846 components between the grains and adjacent to the contacts. When P_p is low (or when σ is high),
847 the increase of pore pressure is expected to be most effective. This qualitatively explains the
848 increase of α with σ, and is consistent with the illustration in Figure 17.
849
850 Although direct measurements of the contact stiffness D_n and D_t are not available and the model
851 is highly idealized, the applicability of this model is of considerable significance. It plausibly
852 explains our observations by considering the interplay between stiff clastic grains and the
853 surrounding compliant components under confining and pore pressure, which highly varies from
854 lithology to lithology.

855

List of Figures:

confining and pore pressures conditions. Note: the depletion and injection data are horizontally offset for differentiation (gray error-bars are for injection data).

Figure 11. Comparison between log data and laboratory measurements. (a) V_P and V_s, (b) Young's modulus, (c) bulk modulus, and (d) derived effective stress coefficient. The laboratory data points are based on confining pressure and pore pressure at 60, and 30 MPa, respectively.

Figure 12. V_P vs. V_s plot of sonic log data (circles) and laboratory measured ultrasonic velocity data (triangles) for each lithological units. Lodgepole (black); Upper Bakken (gray); Middle Bakken (blue); Lower Bakken (gray); Three Forks (red).

Figure 13. Variations of effective stress coefficient for *P*-wave velocities with simple effective stress for constant pore pressures of all six Bakken specimens under both depletion and injection cases.

Figure 14. Variations of effective stress coefficient for *S*-wave velocities with simple effective stress for constant pore pressures of all six Bakken specimens under both depletion and injection cases.

Figure 15. (a) A representative SEM photomicrograph of the microstructure in the Lodgepole specimen (B1V) shows the porous solid matrix and the microcracks; (b) Illustration of a dual-porosity media that generalizes the microstructure shown in (a).

Figure 16. SEM photomicrographs of two silicate-rich specimen thin-sections (B3V and B9V). Thin-sections were prepared orthogonal to bedding planes, which are oriented horizontally. Note the compliant clay (Cl) minerals in between the clastic grains.

Figure 17. Conceptual model of clastic grain surface interactions under low (left) and high (right) confining stress. Dashed contours illustrate the microstructure after alteration due to the confining or pore pressure change as marked. The scale bars qualitatively reflect the contact stiffness.

Figure A1. Comparison of bulk modulus and effective stress coefficient between laboratory dynamic and static measurements. Reference lines (gray) of different ratios are to facilitate comparison.

Figure 1

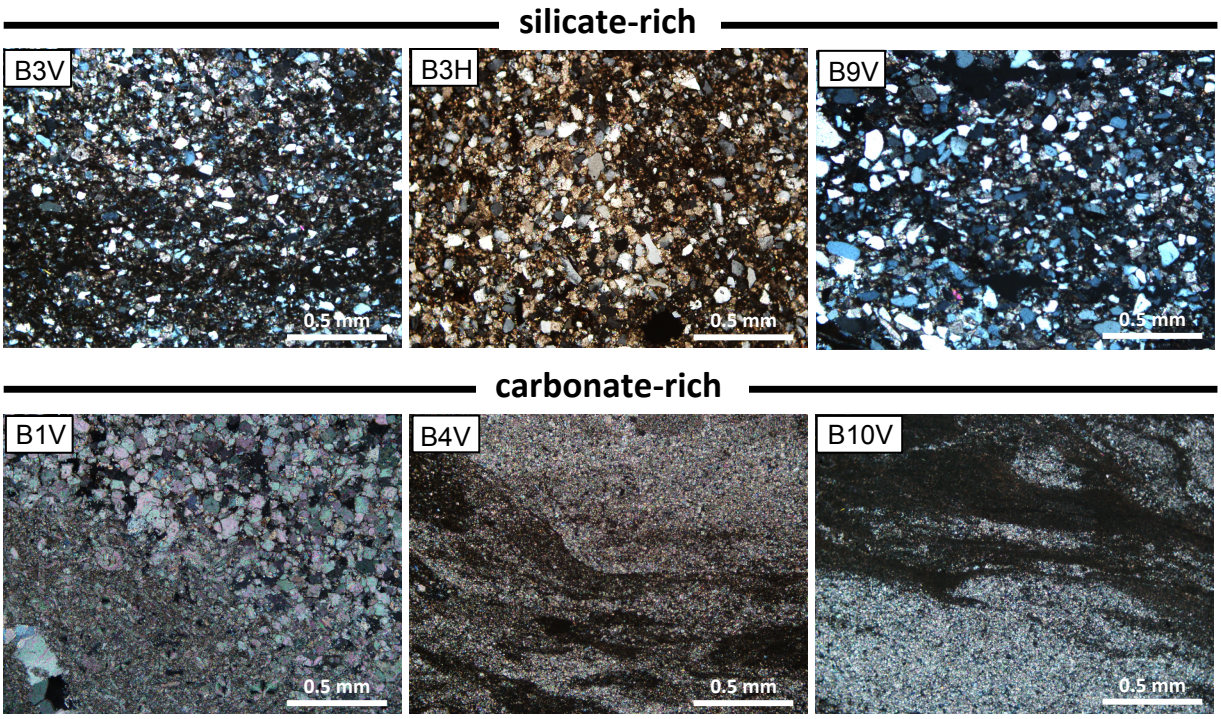

Figure 1. Thin-sections photomicrographs (cross-polarized light) of all six specimens prior to laboratory deformation. Thin-sections are oriented perpendicular to core axes.

Figure 2

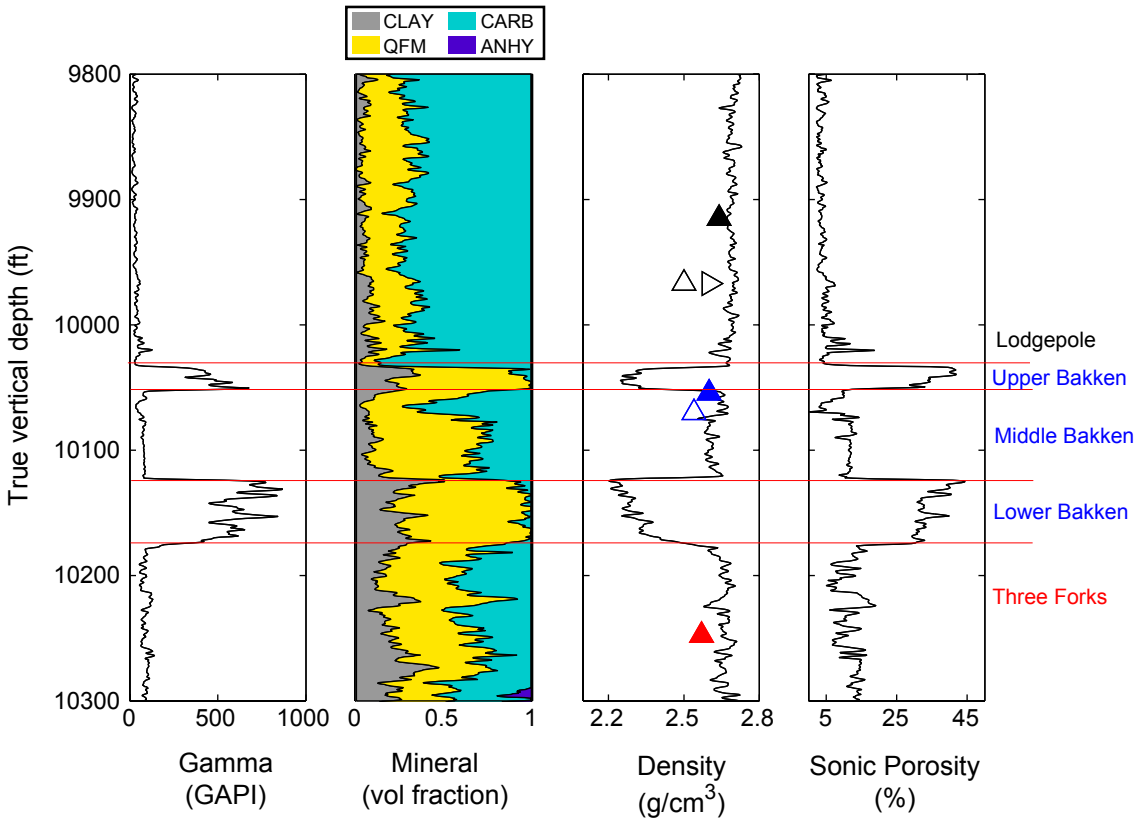

Figure 2. Geophysical logs of the cored vertical well: (a) Natural Gamma Ray log; (b) Elemental Capture Spectrosopy (ECS) log representing the composition of major constintuent minerals (CLAY: clays (plus kerogen); CARB: carbonates; QFM: quartz, feldspar and mica; ANHY: anhydrite) by volume fraction; (c) Density log; (d) Porosity based on dipole sonic log.

Figure 3

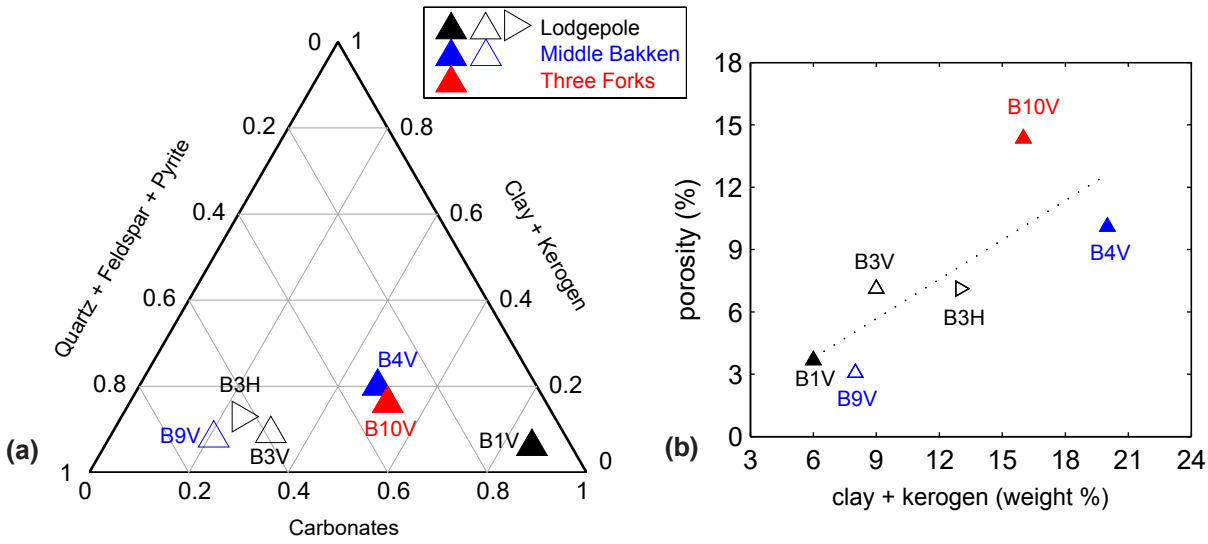

Figure 3. (a) Ternary diagram representing the mineral compositions (in weight fraction) of six Bakken specimens used in this study (from Ma and Zoback, 2017). (b) Correlation between clay plus kerogen weight percent and porosity in all five vertical specimens. The dashed line represents a linear correlation.

Figure 4

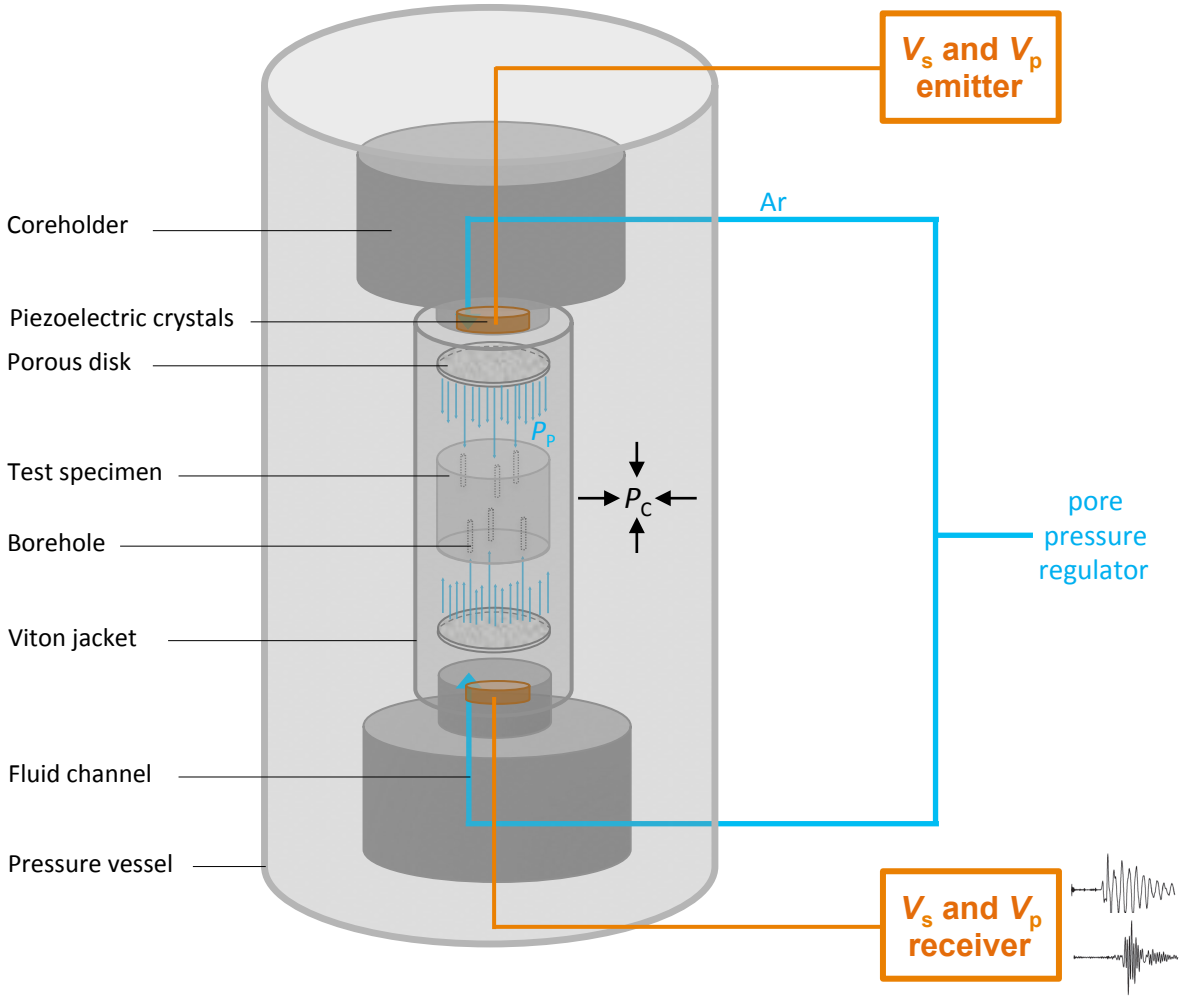

Figure 4. Illustration of the experimental specimen-coreholder assembly housed inside a pressure vessel. The pore fluid flow is indicated by the blue arrows.

Figure 5

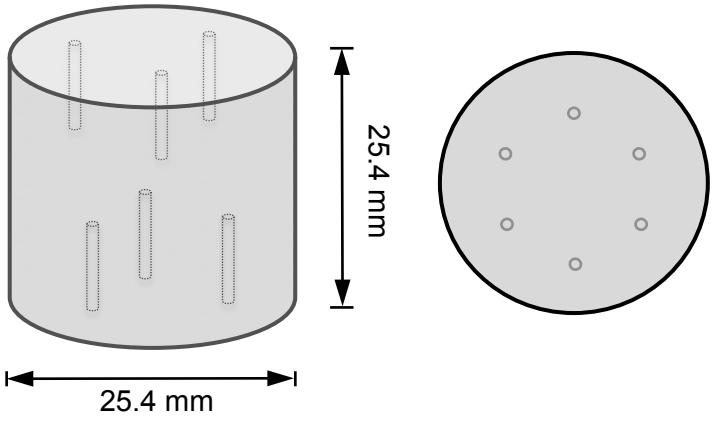

Figure 5. Dimensions of the specimen and the configuration of boreholes drilled inside the specimen.

Figure 6

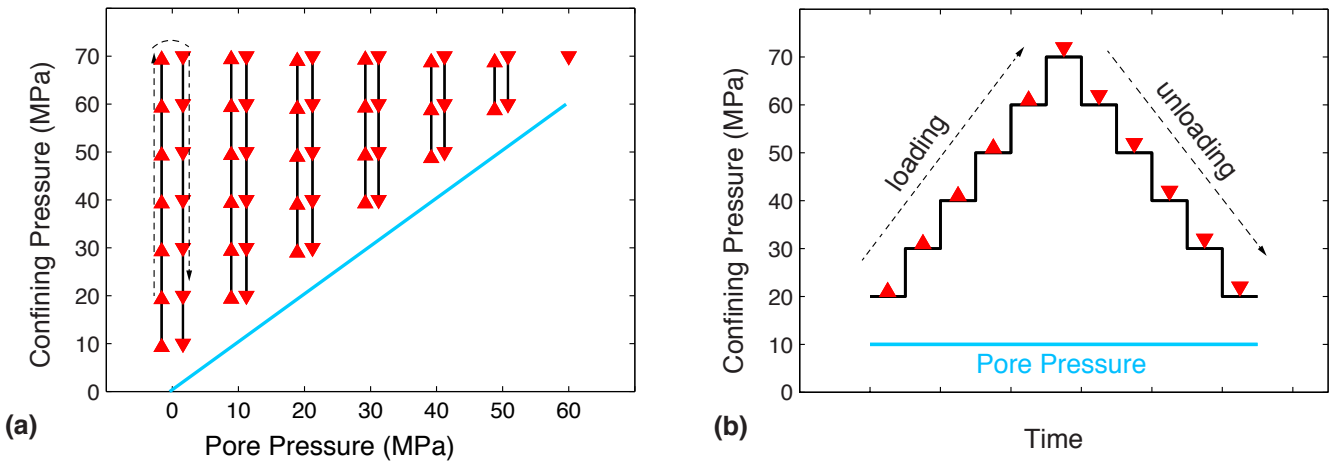

Figure 6. Illustration of the loading path (modified from Ma and Zoback, 2017). (a) All combinations of confining pressure and pore pressure levels. (Each red triangle represents a strain measurement.) (b) Confining pressure is loaded up and down for a constant pore pressure. Note: between each pressure step, sufficient time is allowed for pore pressure equilibrium.

Figure 7

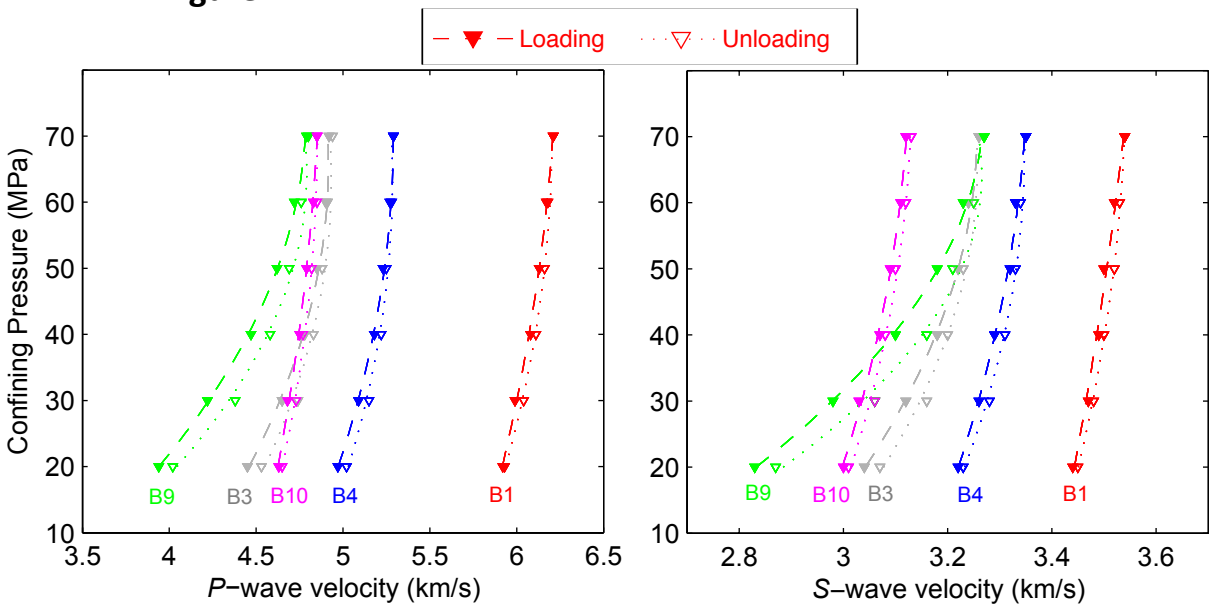

Figure 7. Comparison between the variations of velocity with confining pressure at pore pressure = 10 MPa of all five vertical specimens. (a) P-wave. (b) S-wave.

Figure 8

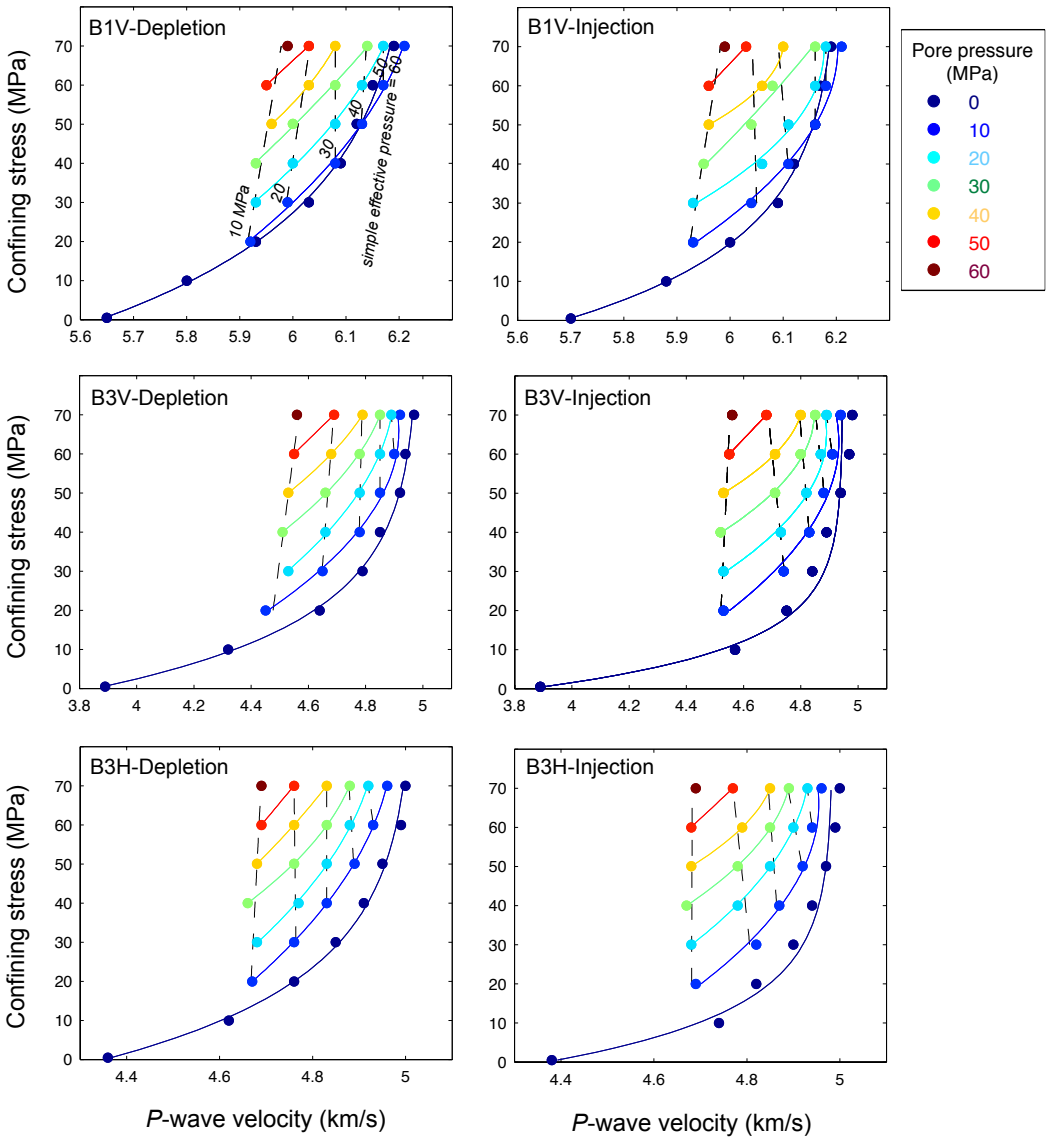

Figure 8. Variations of P-wave velocities with confining pressure for constant pore pressures of all six Bakken specimens. Constant pore pressure (> 0 MPa) data series are fitted by second-order polynomial fitting curves of the corresponding color. Constant simple effective stress data series are fitting by second-order polynomial fitting in dashed black curves.

Figure 8 (continued)

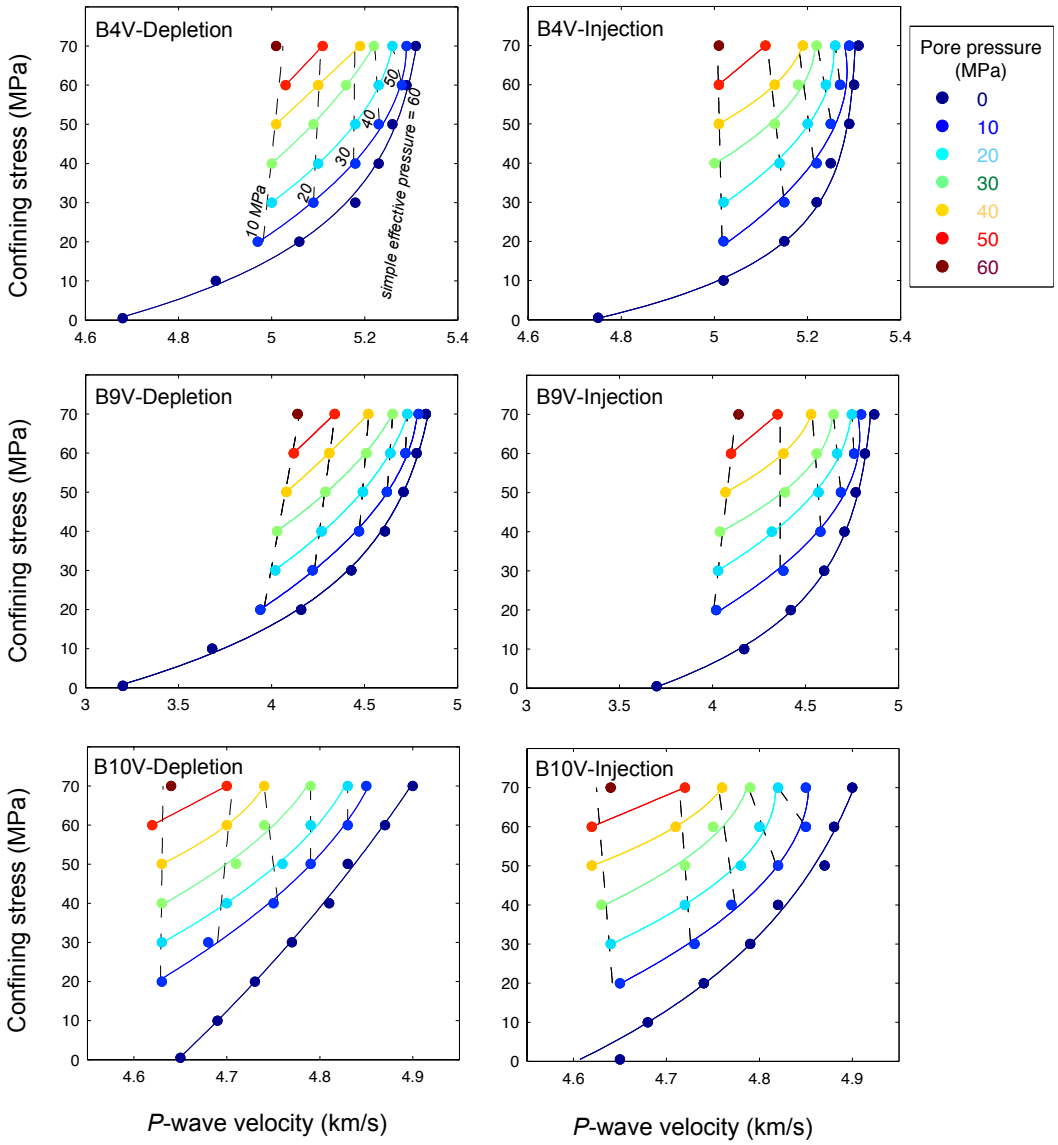

Figure 9

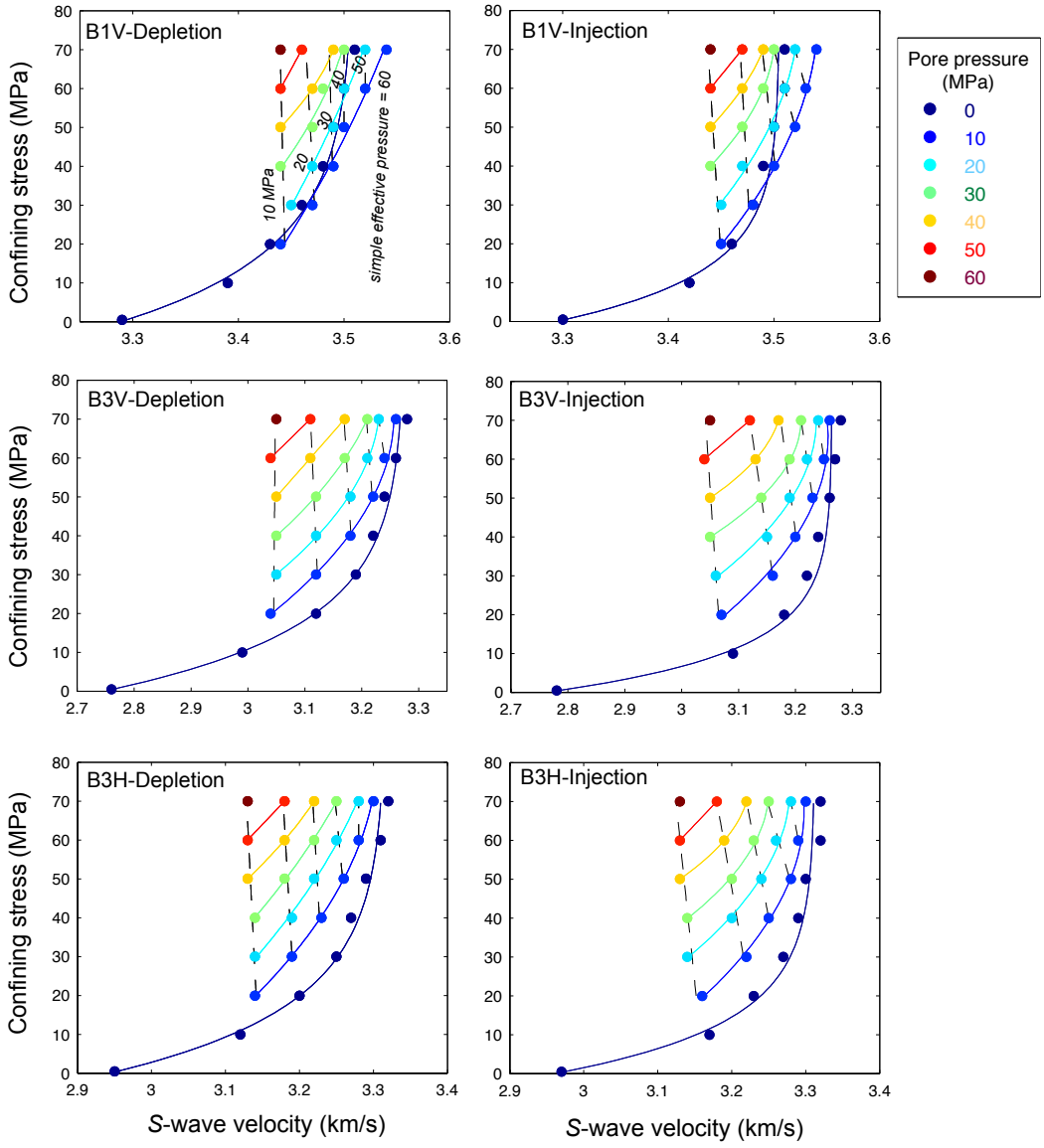

Figure 9. Variations of S-wave velocities with confining pressure for constant pore pressures of all six Bakken specimens. Constant pore pressure (> 0 MPa) data series are fitted by second-order polynomial fitting curves of the corresponding color. Constant simple effective stress data series are fitting by second-order polynomial fitting in dashed black curves.

Figure 9 (continued)

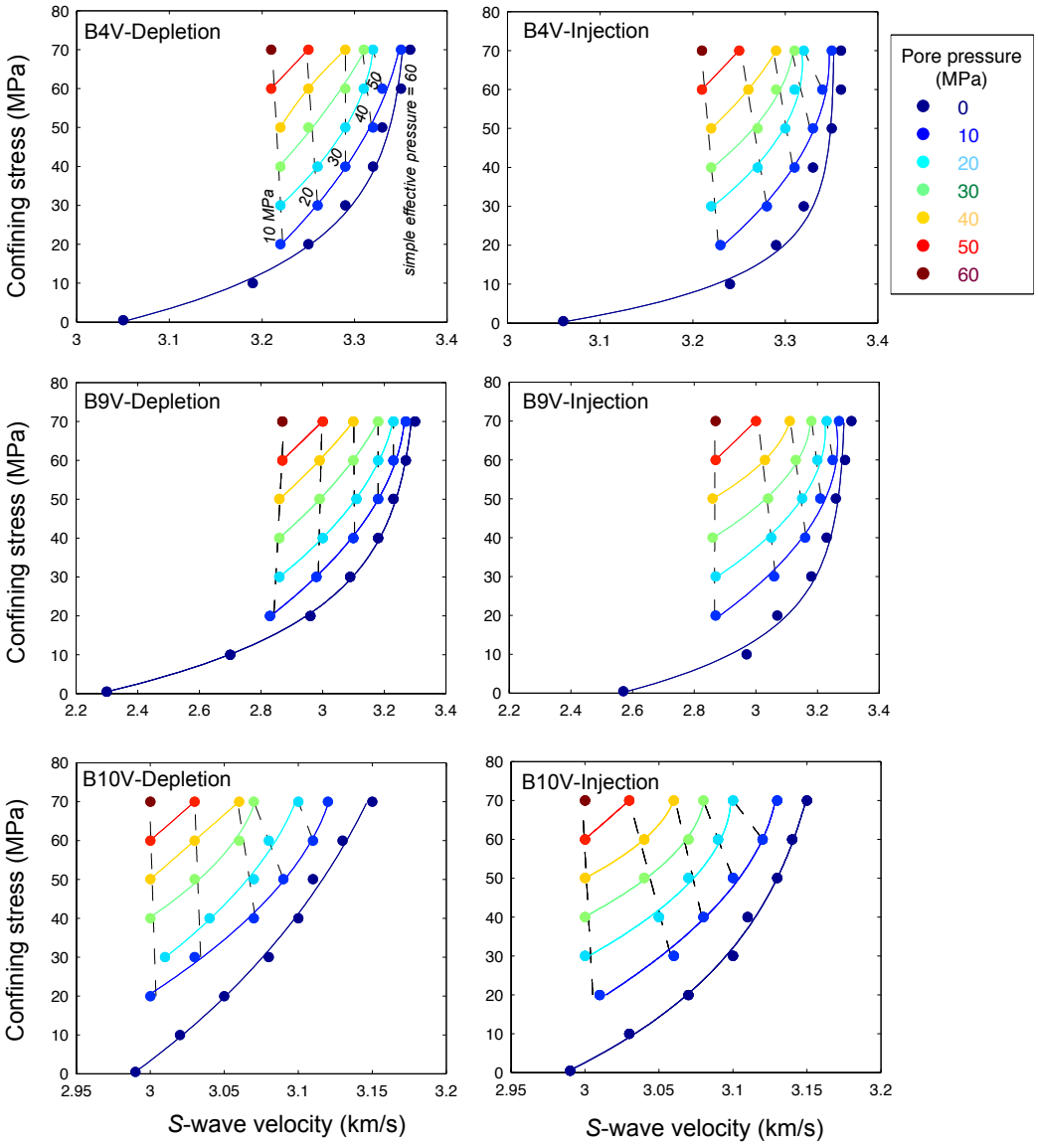

Figure 10

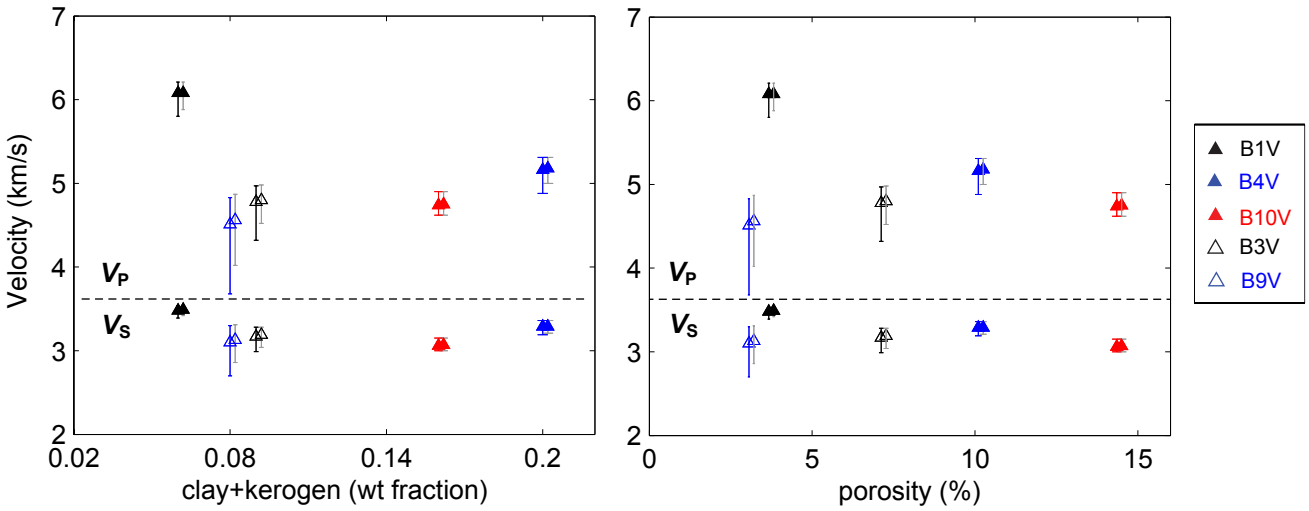

Figure 10. Correlation between velocities and (a) porosity, and (b) clay plus kerogen (weight fraction). The data points represent the velocities when confining pressure and pore pressure at 60, and 30 MPa, respectively. The error-bars reflect the range of the velocities under all applied confining and pore pressures conditions. Note: the depletion and injection data are horizontally offset for differentiation (gray error-bars are for injection data).

Figure 11

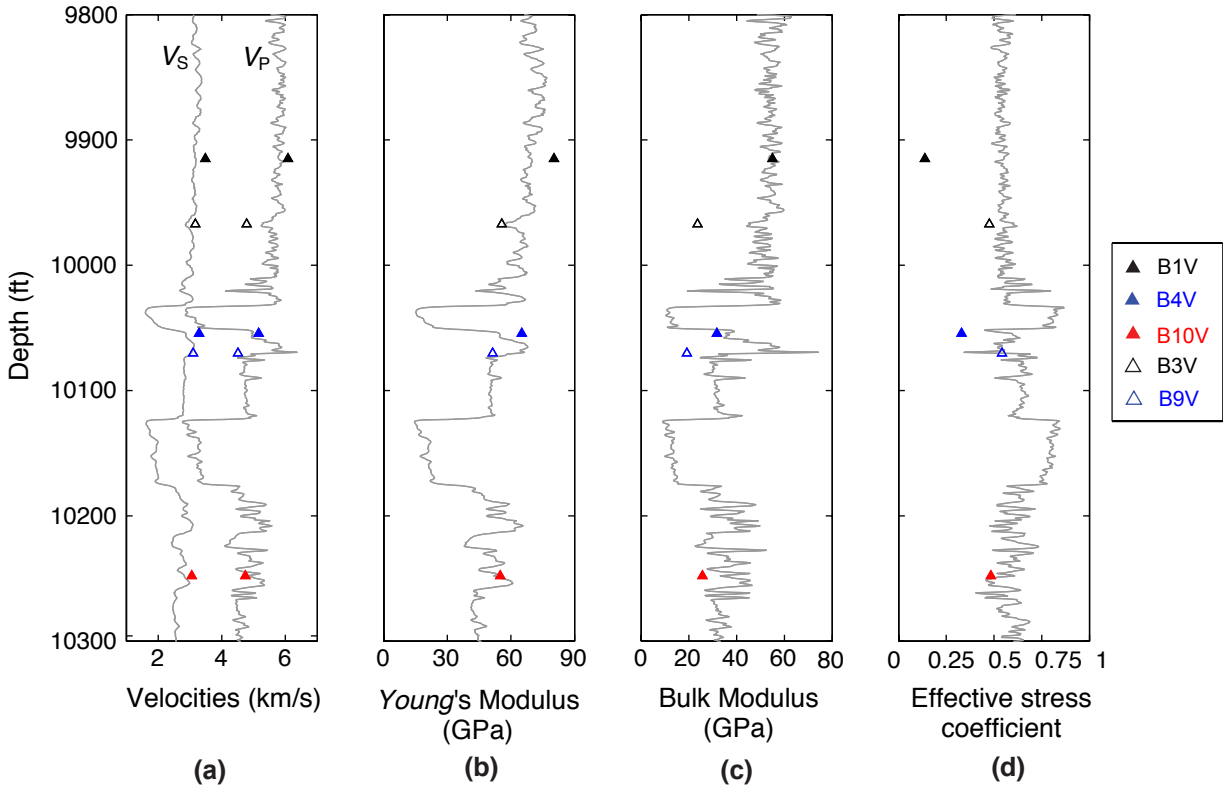

Figure 11. Comparison between log data and laboratory measurements. (a) V_P and V_s, (b) Young's modulus, (c) bulk modulus, and (d) derived effective stress coefficient. The laboratory data points are based on confining pressure and pore pressure at 60, and 30 MPa, respectively.

Figure 12

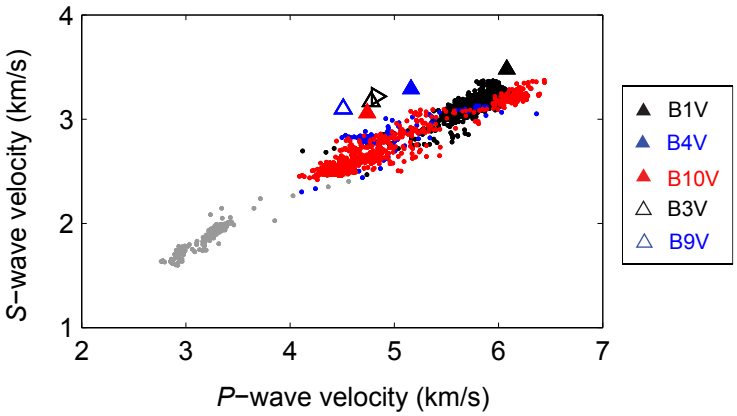

Figure 12. V_P vs. V_s plot of sonic log data (circles) and laboratory measured ultrasonic velocity data (triangles) for each lithological units. Lodgepole (black); Upper Bakken (gray); Middle Bakken (blue); Lower Bakken (gray); Three Forks (red).

Figure 13

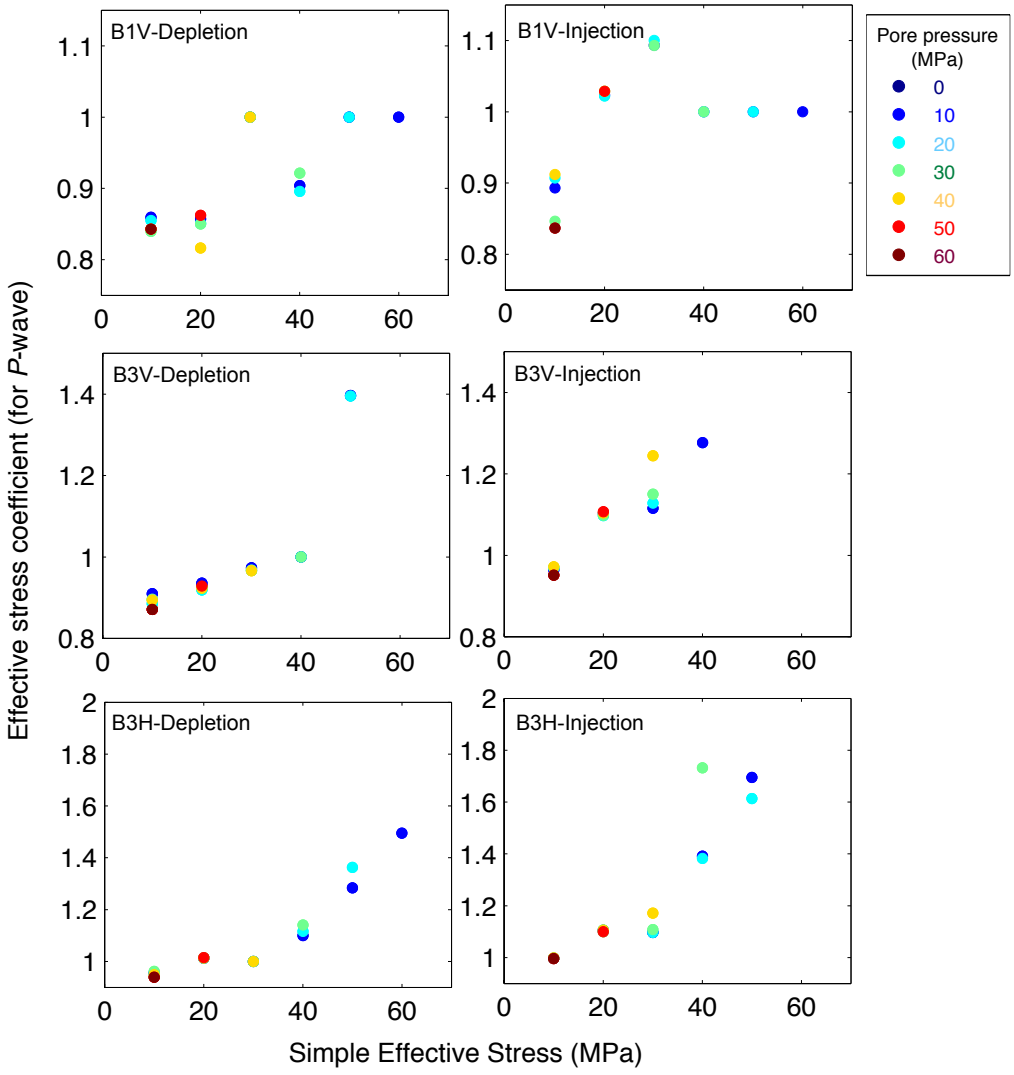

Figure 13. Variations of effective stress coefficient for P-wave velocities with simple effective stress for constant pore pressures of all six Bakken specimens under both depletion and injection cases.

Figure 13 (continued)

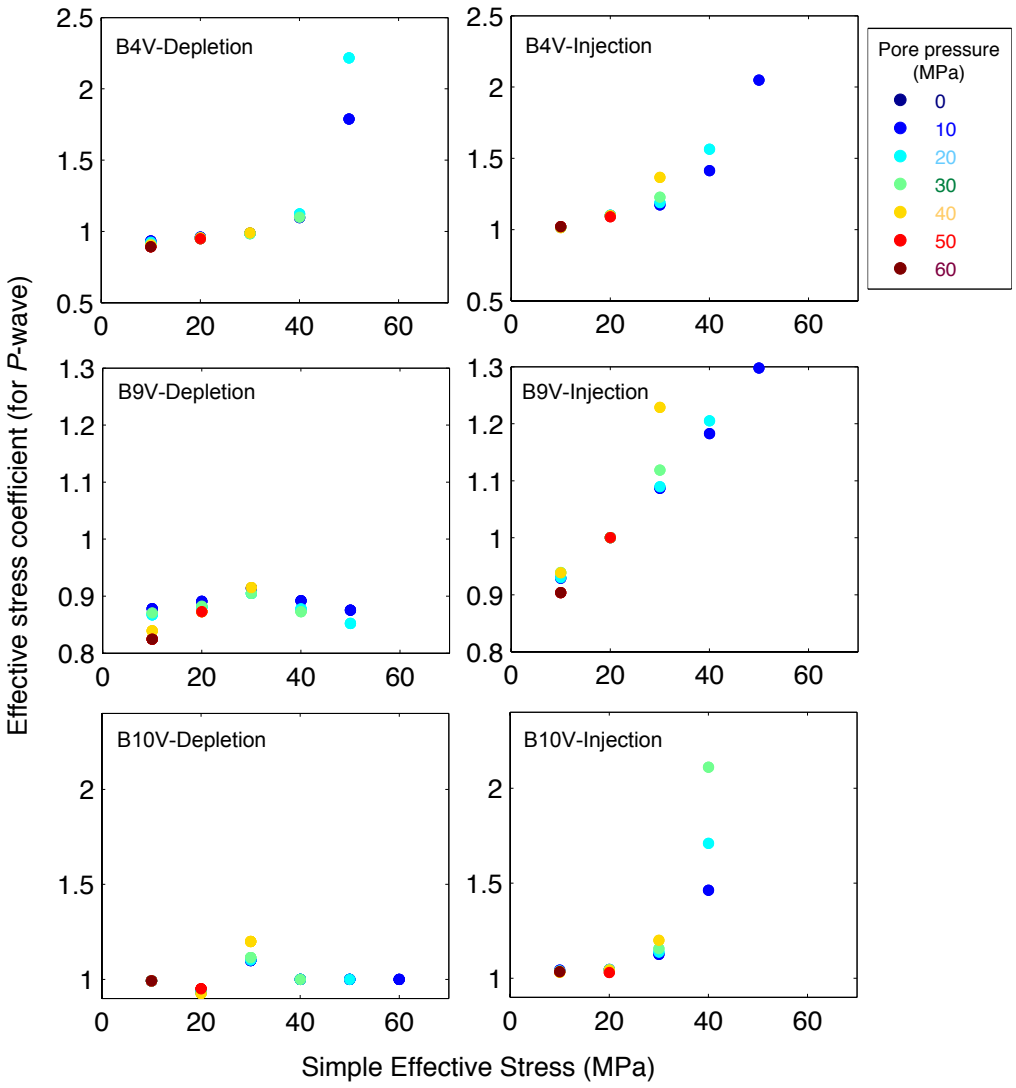

Figure 14

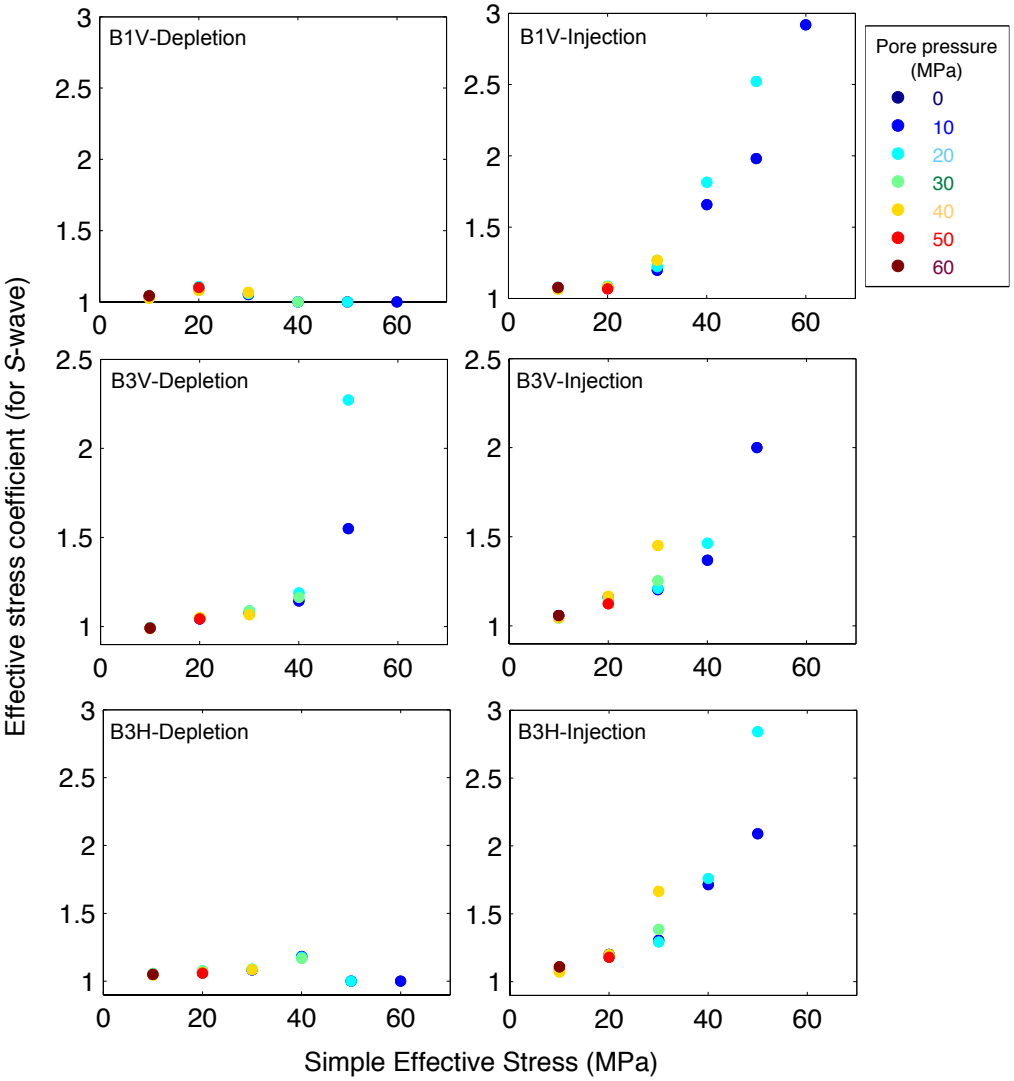

Figure 14. Variations of effective stress coefficient for S-wave velocities with simple effective stress for constant pore pressures of all six Bakken specimens under both depletion and injection cases.

Figure 14 (continued)

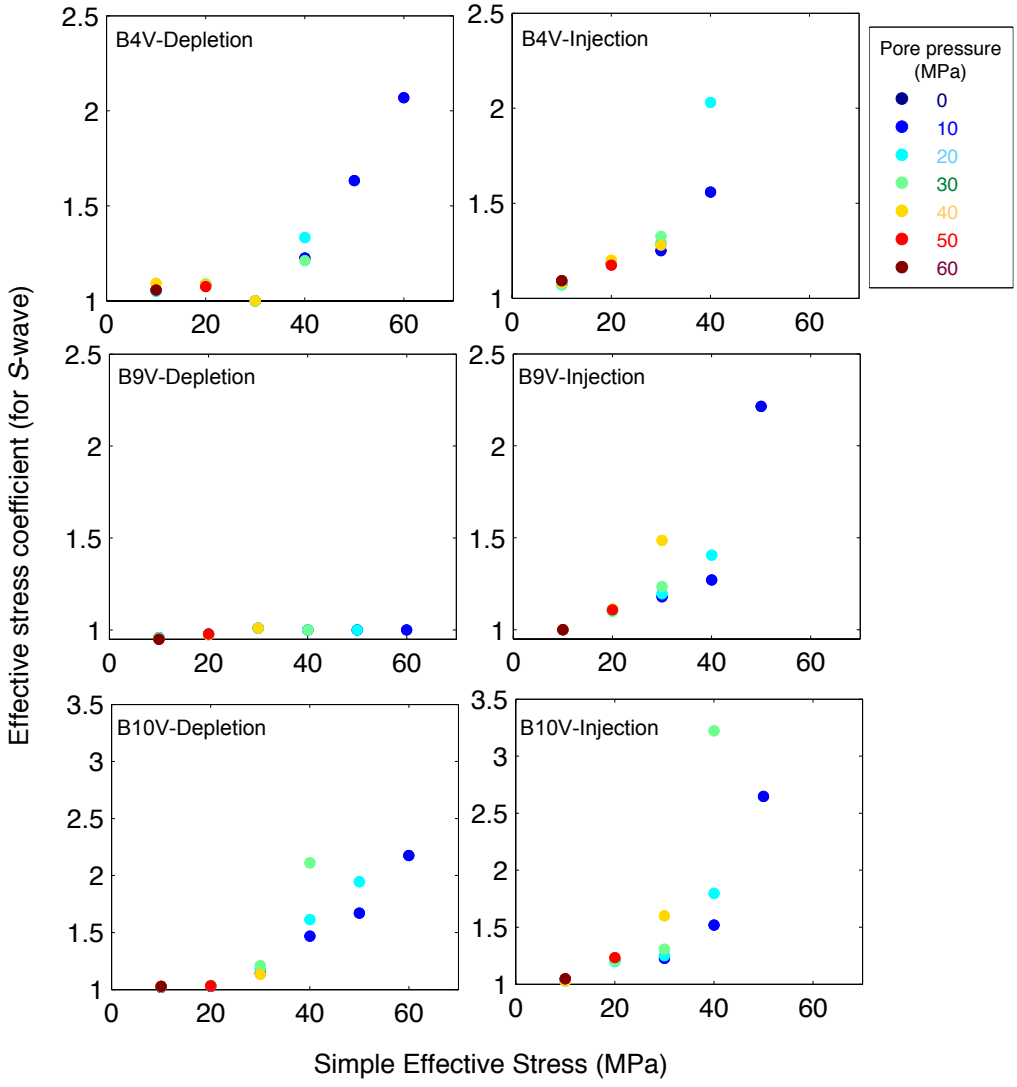

Figure 15

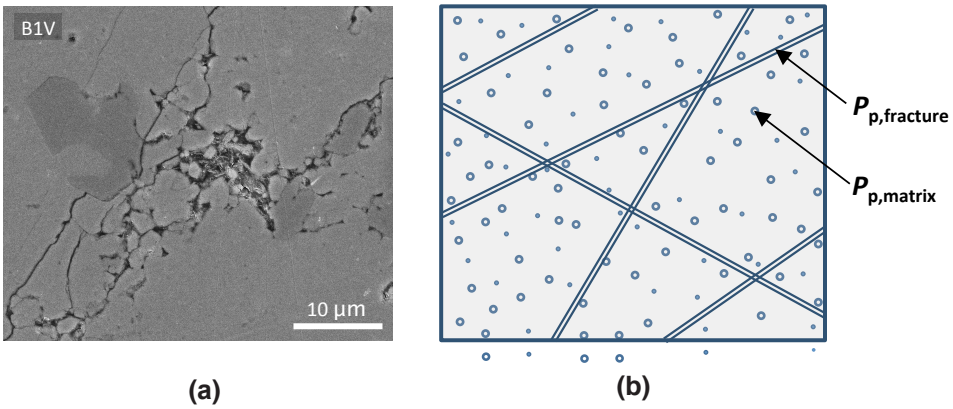

Figure 15. (a) A representative SEM photomicrograph of the microstructure in the Lodgepole specimen (B1V) shows the porous solid matrix and the microcracks; (b) Illustration of a dual-porosity media that generalizes the microstructure shown in (a).

Figure 16

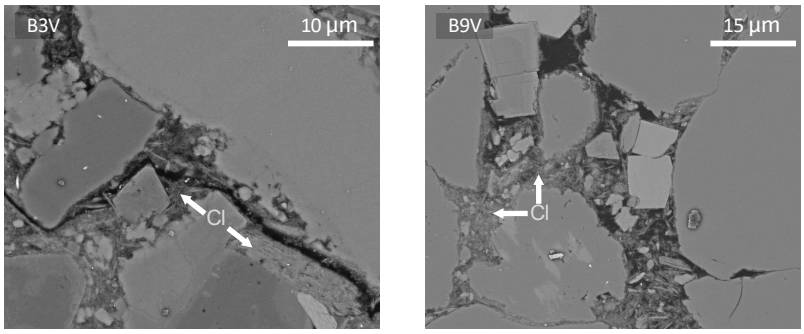

Figure 16. SEM photomicrographs of two silicate-rich specimen thin-sections (B3V and B9V). Thin-sections were prepared orthogonal to bedding planes, which are oriented horizontally. Note the compliant clay (Cl) minerals in between the clastic grains.

Figure 17

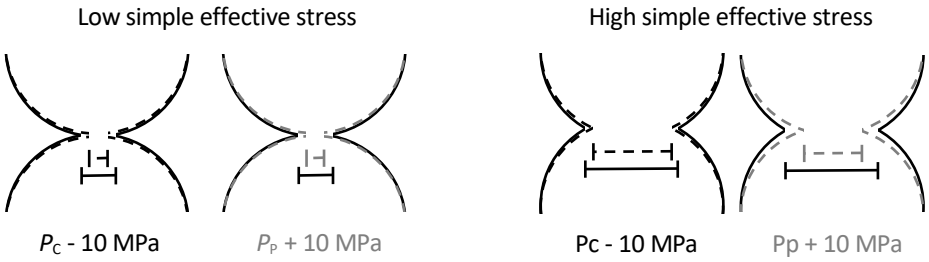

Figure 17. Conceptual model of clastic grain surface interactions under low (left) and high (right) confining stress. Dashed contours illustrate the microstructure after alteration due to the confining or pore pressure change as marked. The scale bars qualitatively reflect the contact stiffness.

Figure A1

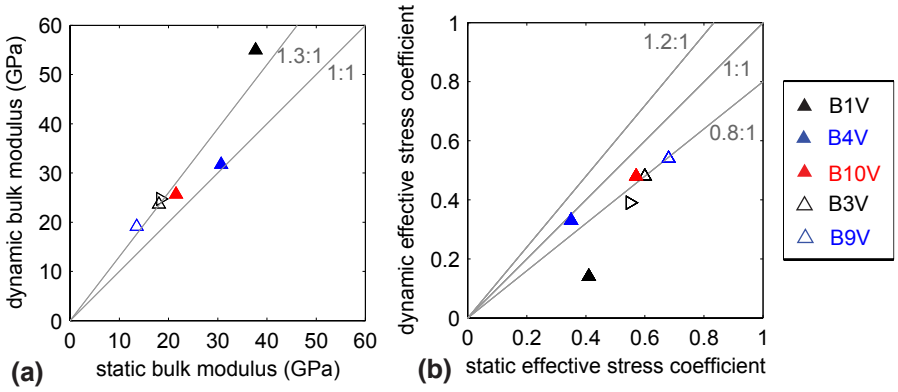
dynamic bulk modulus (GPa)
static bulk modulus (GPa)
1.3:1
1:1
(a)
dynamic effective stress coefficient
static effective stress coefficient
1.2:1
1:1
0.8:1
(b)
B1V
B4V
B10V
B3V
B9V

Declaration of interests

 The authors declare that they have no known competing financial interests or personal relationships that could have appeared to influence the work reported in this paper.

☐The authors declare the following financial interests/personal relationships which may be considered as potential competing interests: